MACHINE LEARNING BASED FEASIBILITY ANALYSIS OF GEOTHERMAL BRIDGE DECK DEICING SYSTEMS IN MONTANA

by

Syed Haider Ali Sherazi

A thesis submitted in partial fulfillment
of the requirements for the degree

of

Master of Science

in

Civil Engineering

MONTANA STATE UNIVERSITY
Bozeman, Montana

May 2025

©COPYRIGHT

by

Syed Haider Ali Sherazi

2025

All Rights Reserved

DEDICATION

This thesis is dedicated to my parents with deepest love and gratitude. From the very beginning, you have been my pillars of strength, my greatest supporters, and my most patient teachers. This accomplishment is not mine alone, it reflects your unconditional support and boundless love. Thank you for everything.

ACKNOWLEDGEMENTS

I would like to express my gratitude to my committee chair, Dr. Mohammad Khosravi, for his invaluable guidance, mentorship, and unwavering support throughout the course of my research and writing. His expertise, patience, and insightful feedback have played a vital role in shaping this thesis.

Dr. Khosravi's encouragement pushed me to think critically, work diligently, and strive for excellence in every stage of this journey. His genuine dedication to both research and teaching has been a great source of inspiration, and I feel truly fortunate to have worked under his guidance.

Thank you, Dr. Khosravi, for believing in me and for helping me grow not only as a researcher but also as a person.

TABLE OF CONTENTS

1. INTRODUCTION AND BACKGROUND 1

Introduction 1
Overview 4
Outline 6

2. DATA COLLECTION AND SIMULATIONS 8

Introduction 8
Data Collection and Preprocessing 10
Meteorological Data 11
Ambient Temperature 11
Wind Speed 13
Solar Radiation 14
Ground Temperature 15
Ground Properties 17
Numerical Model Development 18
Overview of the experiments: 19
Overview of Numerical Model 20
Model Validation: 22
Parametric Study 25
Ambient Temperature 26
Wind Speed 27
Solar Radiation 28
Inlet Temperature 29
Flow Rate 30
Tube Spacing 31
Bridge Length 32
Effect of Solar, Inlet Temperature, and Tubing 33

3. MACHINE LEARNING MODEL DEVELOPMENT 35

Introduction 35
Prediction Model Development Framework 35
Machine Learning Model Development Process 36
Step 1: Feature Selection 38
Step 2: Data Generation 39
Step 3: Data Splitting and Experimental Design 42
Step 4: Model Selection and Training 43
Step 5: Model Evaluation 45
Mean Absolute Error (MAE) 45
Root Mean Squared Error (RMSE) 45

TABLE OF CONTENTS CONTINUED

Coefficient of Determination (R^2) 46
Model 1 46
Model 2 51
Step 6: Feature Importance Analysis 54
Temperature Prediction Interactive Tool 56
Summary 58
Future Work 60

REFERENCES CITED 62

APPENDICES 66

EXPERIMENTAL BRIDGE DECK SCHEMATIC 67

DETERMINISTIC ANALYSIS 69

LIST OF TABLES

Tables Page

1. Table 1: Material properties of the numerical model 21
2. Table 2: Properties of baseline model for parametric studies 26
3. Table 3: Properties of baseline model for feature sensitivity 38
4. Table 4: Different levels of percentiles for empirical values and fitted distributions for ambient temperature, wind speed, and solar radiation 41
5. Table 5: Mean and standard deviation of fitted distributions for inlet temperature 41
6. Table 6: Parameter ranges, combinations and total number of models for generating the dataset without tubing from the numerical model 41
7. Table 7: Parameter ranges, combinations and total number of models for generating the dataset with tubing from the numerical model 42
8. Table 8: Input features and target variables for machine learning model 1 and model 2 43
9. Table 9: MAE, RMSE, and R^2 score values for Model 1 without tubing for Stabilized temperature, time to reach stabilized temperature, and time to reach above 0^{o}C 48
10. Table 10: MAE, RMSE, and R^2 score values for Model 1 with tubing for Stabilized temperature, time to reach stabilized temperature, and time to reach above 0^{o}C 50
11. Table 11: MAE, RMSE, and R^2 score values for Model 2 output without tubing 52
12. Table 12: MAE, RMSE, and R^2 score values for Model 2 output with tubing 54
13. Table B1: QBHE Variables 70
14. Table B2: System Installation Costs 70
15. Table B3: Environmental Analysis Results 70

LIST OF FIGURES

Figure Page

1. Figure 1: Heat transfer mechanisms in bridge deck (Turner et al., 2024) 9
2. Figure 2: (a) Map of bridges and major roads, and (b) electric transmission lines locations in Montana 11
3. Figure 3: (a) Locations of MDT RWIS sites (map source: https://roadreport.mdt.gov/), (b) average ambient temperature distribution histogram for Montana, and (c) time series of ambient temperatures for 2016–2019 (site ID 150000) 12
4. Figure 4: Heat map of average annual temperature in Montana using Kriging interpolation 13
5. Figure 5: (a) Frequency distribution of wind speeds in Montana, and (b) spatial distribution of the coefficient of variation of wind speeds across Montana 14
6. Figure 6: Frequency distribution of shortwave solar radiation in Montana 15
7. Figure 7: Ground temperature characteristics across Montana: (a) normalized frequency distribution of ground temperatures, (b) ground temperature versus depth, and (c) spatial distribution of ground temperatures and well locations 17
8. Figure 8: Soil thermal properties across Montana: (a) spatial distribution of thermal conductivity based on USGS soil classification, and (b) spatial distribution of thermal capacity based on USGS soil classification 18
9. Figure 9: Experimental model configuration with sensor locations: (a) plan view; and (b) section views (Turner et al., 2024) 20
10. Figure 10: Overview of the numerical model: (a) numerical model configuration, and (b) meshed model in COMSOL Multiphysics (Turner et al., 2024) 22
11. Figure 11: (a) synthetic scenario test plan, (b) daily fluctuation scenario test plan, (c) synthetic scenario validation, and (d) daily fluctuation scenario validation 25

LIST OF FIGURES CONTINUED

Figure Page

12. Figure 12: Influence of ambient temperature on surface temperature and heating time 27

13. Figure 13: Influence of wind speed on surface temperature response 28

14. Figure 14: Influence of solar radiation intensity on bridge surface temperature 29

15. Figure 15: Surface temperature response for different inlet fluid temperatures 30

16. Figure 16: Influence of fluid flow rate on surface temperature and heating efficiency 31

17. Figure 17: Impact of tube spacing on surface temperature distribution 32

18. Figure 18: Surface temperature profiles for varying bridge lengths 33

19. Figure 19: Bridge deck surface temperature with and without solar radiation, for different inlet temperatures 34

20. Figure 20: Machine learning model development process 37

21. Figure 21: Effect of various parameters on bridge deck average surface temperature: (a) without tubing, and (b) with tubing 39

22. Figure 22: Distribution histograms of important features, a) Ambient temperature, b) Wind speed, c) Solar radiation, and d) Inlet temperature 41

23. Figure 23: Schematic for stabilized temperature, time to reach stabilized temperature, and time to reach above 0^{o}C 44

24. Figure 24: Outputs from Model 1 and Model 2 44

25. Figure 25: MAE, RMSE, and R^2 score comparison for Model 1 without tubing for Stabilized temperature, time to reach stabilized temperature, and time to reach above 0^{o}C 48

26. Figure 26: MAE, RMSE, and R^2 score comparison for Model 1 with tubing for Stabilized temperature, time to reach stabilized temperature, and time to reach above 0^{o}C 50

LIST OF FIGURES CONTINUED

Figure Page

27. Figure 27: MAE, RMSE, and R^2 score comparison for Model 2 output without tubing 52

28. Figure 28: MAE, RMSE, and R^2 score comparison for Model 2 output with tubing 54

29. Figure 29: Permutation-based feature importance for FCNN model predictions visualized as radar plot: a) without tubing, and b) with tubing 56

30. Figure 30: Interactive map of Montana showing bridge deck locations 56

31. Figure 31: Input parameters interface for: (a) fixed parameters, and (b) variable parameters 57

32. Figure 32: Predicted surface temperature over time for a two-segment “with tubing” scenario 58

33. Figure A1: Tubing configuration in bridge deck a) top view, and b) 3D view 68

34. Figure A2: Sensor configuration in bridge deck a) top view, and b) cross section view 68

ABSTRACT

Bridge decks in cold climate regions such as Montana are especially vulnerable to rapid freezing, snow accumulation, and thermal-induced cracking due to their exposure to ambient conditions on all sides. Traditional deicing methods, relying on chemical salts and plowing, are costly, environmentally harmful, and often ineffective at extreme temperatures. As a sustainable alternative, geothermal bridge deck deicing systems utilizing ground-source heat pumps (GSHPs) have captured growing interest due to their ability to provide continuous, low-energy heating. However, widespread implementation across Montana requires a comprehensive understanding of system performance across the state's diverse climatic and geological conditions. This thesis presents an integrated framework that combines numerical modeling, machine learning (ML), and geographic information systems (GIS) to assess the technical, economic, and environmental feasibility of GSHP-based bridge deck deicing systems. Numerical simulations were conducted using COMSOL Multiphysics, calibrated against experimental data, to evaluate the effects of ambient temperature, wind speed, solar radiation, inlet fluid temperature, flow rate, tube spacing, and bridge length on surface temperature response. These simulations generated a dataset of over 2,000 scenarios used to train and validate several ML models, including Random Forest, XGBoost, and fully connected neural networks (FCNN). The models achieved R^2 scores above 0.95 and enabled rapid, high-accuracy prediction of key outputs such as surface temperature, time to de-ice, and time to reach stabilized temperature. GIS-based statewide feasibility analysis was performed, and spatial datasets of geothermal potential, energy demand, borehole depth, installation cost, and environmental impact were evaluated to identify high-potential implementation zones. Results show that GSHP systems are feasible across most of Montana, particularly in regions with high subsurface thermal gradients. This work demonstrates that machine learning, when combined with simulation and geospatial data, provides a powerful and scalable tool for evaluating the feasibility of renewable infrastructure technologies. The findings support the strategic deployment of GSHP systems at key bridge locations and offer a replicable framework for sustainable infrastructure planning in other cold-region environments.

CHAPTER ONE

INTRODUCTION AND BACKGROUND

Introduction

Winters in Montana can vary from mild to extreme, with monthly average ambient temperatures ranging between -12.1°C and 22.6°C. These conditions, coupled with severe winter storms that can deposit up to 40 inches of snow across the state, often lead to significant accumulations of ice and snow on roadways. This presents major safety concerns, as icy roads are a leading cause of vehicle accidents. Notably, "the average icy road fatality counts 3.6 times the total deaths from all other weather hazards combined," with an annual nationwide average of 536,731 crashes (Robinson, 2021). The buildup of ice and snow is especially problematic on bridges, as their elevated surfaces are exposed to colder ambient air temperatures from all sides, unlike most road surfaces, which benefit from warmer ground temperatures. Additionally, bridges are often designed with narrower road widths to facilitate vehicle passage over obstacles like water bodies, which can further increase the consequences of crashes.

Currently, Montana has two primary methods for maintaining roads affected by ice and snow (Williams, 2003). The first method involves using traction sand to increase friction on slick surfaces. While this method does not reduce the quantity of snow and ice, it provides a drivable surface for vehicles. However, it is inefficient during heavy winters, as it must be reapplied after every storm (Fay et al., 2015). This approach also poses risks to workers who must drive on slick roads to apply the sand. Despite its limitations, it is often the only viable option in extremely cold weather. The second method involves applying sodium and magnesium chlorides to melt the ice.

Like traction sand, these salts must be reapplied after major winter events. Their effectiveness diminishes at low temperatures, with magnesium chloride working only above -12.2°C and sodium chloride above -9.5°C (MDT Web Administrators, 2019). While these chlorides improve driver safety, they can negatively impact infrastructure and the environment. During the melting season, the chlorides can infiltrate cracks in the bridge deck, increasing corrosion and reducing the bridge's lifespan. They can also enter natural ecosystems, causing ecological disruptions. Frequent storm events during Montana winters make this maintenance approach costly (Erickson, 2018).

Recently, new materials and innovative technologies, such as hydronic heating systems, have been introduced to mitigate ice and snow accumulation on transportation infrastructure. Among the proposed heated pavement systems, electrically heated and hydronically heated pavements are the most common. While electrically heated pavements can be implemented wherever power is available, their high voltage requirements and operational costs have limited widespread adoption (Fliegel et al., 2010). In contrast, hydronic heating systems for snow and ice removal on bridge decks have gained increasing attention. These systems extract heat from shallow or deep earth layers through thermo-active foundations or boreholes, relying on mechanisms of heat transfer including convection, conduction, and radiation (Lund & Boyd, 2016). Since ground temperature fluctuations are minimal at depths of approximately 6–9 meters (20–30 feet) (Kusuda & Achenbach, 1965), geothermal loops installed at these depths provide an efficient alternative to piles and wells for harvesting geothermal energy through ground heat exchange. The geothermal energy harvested from the ground can be utilized for de-icing bridge decks during winter months. In addition to snow and ice removal, hydronically heated pavement systems can moderate surface temperature fluctuations and reduce thermal stresses within the concrete, thereby minimizing the

risk of expansion-related cracking. Although geothermal bridge deck deicing systems show considerable potential, their design and implementation remain highly site-specific due to the complex interplay of local climate, subsurface thermal properties, and bridge geometry. The performance of geothermal bridge deck deicing systems is influenced by multiple factors, including material properties (e.g., thermal conductivity of soil and concrete) and system design parameters such as inlet fluid temperature, pipe embedment depth, and pipe spacing. System efficiency improves with higher inlet fluid temperatures and increased concrete thermal conductivity. Conversely, greater pipe embedment depths and wider pipe spacing negatively affect system performance (Ghasemi-Fare & Basu, 2016).

Several prior studies have attempted feasibility assessments. Yu et al. (2025) conducted a comprehensive multi-phase study in Texas that encompassed laboratory-scale slab tests, mock-up field demonstrations, and implementation on an in-service bridge. The research not only optimized system design using FEM simulations but also evaluated operational performance during real winter events. The study linked geothermal deicing to improved safety by demonstrating effective snow and ice removal during extreme cold events, reducing freezing surface hours, and thereby mitigating accident risks. The life-cycle cost-benefit analysis concluded that the system is economically viable, especially for high-traffic bridges, due to substantial long-term savings from reduced corrosion damage, fewer crash-related delays, and improved winter travel safety. McNamara et al. (2025) assessed the feasibility of implementing ground source heat pump (GSHP) systems for bridge deck deicing in winter and deck cooling in summer across Montana. Their analysis comprised three main components: (1) energy feasibility, evaluating the availability of shallow geothermal resources and the thermal energy demand for seasonal bridge temperature

regulation; (2) economic viability, estimating borehole drilling requirements, installation costs, and the long-term operational costs of GSHPs; and (3) environmental impact, quantifying the potential reductions in chloride use and associated carbon dioxide (CO_2) emissions. The findings suggest that GSHPs are technically feasible, economically promising, and environmentally advantageous, particularly in regions with high geothermal potential, such as southwest Montana. However, the economic analysis primarily considers installation and energy costs without accounting for potential variability in material prices, maintenance needs, or lifecycle system degradation. Similarly, the environmental assessment is limited in scope—it estimates average reductions in chloride and CO_2 emissions but does not fully capture the broader ecological or watershed impacts. Despite these limitations, the study highlights that reduced salt usage may extend bridge service life and lessen environmental harm, positioning GSHPs as a viable strategy for sustainable bridge maintenance. Moreover, the energy feasibility component is based on deterministic analyses using long-term average annual temperature and climate data, which may not reflect seasonal extremes or future climate variability. This approach does not fully capture the transient thermal behavior of the ground or the dynamic operational demands of GSHP systems during extreme weather events. As such, further studies incorporating transient simulations, uncertainty quantification, and site-specific system design are needed to improve the robustness of GSHP implementation strategies for bridge deck applications.

Overview

This research focuses on developing a machine learning-based predictive modeling framework for evaluating the thermal performance of geothermal bridge deck systems under varied environmental and design conditions. Building upon validated numerical simulations, the

objective is to create rapid, accurate, and scalable prediction tools that can emulate the thermal response of bridge decks without relying on computationally expensive numerical models. The predictive models developed through this work aim to support future design, evaluation, and optimization of geothermal bridge deicing systems, particularly in cold climates like Montana.

The study begins with the development of a validated numerical model in COMSOL Multiphysics. This model simulates the heat transfer mechanisms within bridge decks equipped with ground source heat pump (GSHP) systems, capturing conductive, convective, and radiative heat exchanges with the surrounding environment. Model development is informed by experimental testing results, ensuring that both thermal and structural responses are realistically represented. A wide range of environmental conditions and design parameters, including ambient temperature, wind speed, solar radiation, inlet fluid temperature, flow rate, tube spacing, and bridge length, are incorporated into the simulation framework to generate a comprehensive dataset.

A total of more than 2,000 numerical simulations are performed to generate datasets representing realistic operating conditions for geothermal bridge decks. Two distinct machine learning models are developed from these datasets. Model 1 is designed to predict summary performance indicators, including stabilized surface temperature, time to reach above 0°C, and time to reach stabilized temperature. Model 2 provides detailed predictions of surface temperature profiles at fine time intervals, enabling dynamic monitoring of bridge deck thermal behavior.

Multiple supervised machine learning algorithms are trained and evaluated, including linear regression, polynomial regression, decision trees, random forests, XGBoost, and fully connected neural networks (FCNN). Model performance is assessed using mean absolute error (MAE), root mean squared error (RMSE), and coefficient of determination (R^2). Feature

importance and sensitivity analyses are conducted to interpret model predictions and to identify the most influential variables governing surface temperature outcomes. Across the various models tested, XGBoost performed comparatively better for predicting summary metrics (Model 1), while the FCNN performed better for predicting time-dependent surface temperature profiles (Model 2).

Outline

This thesis is organized into four chapters, each systematically addressing different aspects of the research objectives.

Chapter 1 introduces the research motivation, highlighting the critical issues associated with bridge deck icing, the limitations of traditional deicing methods, and the potential of geothermal systems as a sustainable alternative. It reviews previous feasibility studies, including work conducted for Texas by Yu et al. (2025) and the deterministic GIS-based feasibility analysis for Montana by McNamara et al. (2025). The chapter concludes by presenting an overview of the research approach and the structure of the thesis.

Chapter 2 focuses on data collection and numerical simulation development. It begins with a discussion of heat transfer mechanisms relevant to bridge deck performance under geothermal heating. It then describes the meteorological and ground data collected for Montana, including ambient temperature, ground temperature, and soil thermal properties. The chapter further details the development of a validated numerical model based on COMSOL Multiphysics, drawing on experimental bridge deck testing reported by Turner et al. (2024). The model's configuration, heat transfer boundary conditions, meshing strategies, and validation against experimental results are discussed to establish confidence in its predictive capabilities.

Chapter 3 presents the machine learning model development. It introduces a structured six-step framework for prediction model creation, encompassing feature selection, dataset generation through automated numerical simulations, data splitting, model selection and training, model evaluation, and feature importance analysis. Two machine learning models are developed: Model 1 predicts system-level performance indicators, while Model 2 forecasts full surface temperature profiles. Various machine learning algorithms, including linear regression, decision trees, random forests, XGBoost, and fully connected neural networks (FCNN), are trained and compared based on MAE, RMSE, and R^2 metrics. Feature importance and sensitivity analyses are conducted to enhance interpretability and understand system behavior under varying conditions.

Chapter 4 concludes the thesis with a summary of key findings and discusses directions for future work. It highlights the contributions of the research to geothermal deicing system design and predictive modeling, discusses practical implications for infrastructure management, and outlines potential areas for extending the work, including real-time implementation, hybrid simulation-ML modeling approaches, and broader applications across other cold regions.

CHAPTER TWO

DATA COLLECTION AND SIMULATIONS

Introduction

The geothermal bridge deck deicing system was simulated using a three-dimensional (3D) numerical model developed in COMSOL Multiphysics. Figure 1 presents the fundamental heat transfer mechanisms considered (conduction, convection, and radiation) in the bridge deck model. The primary modes of heat transfer incorporated in the model include conduction within the concrete and heat exchanger tubing, convection at the exposed bridge deck surfaces, and thermal radiation exchange with the environment. Conduction governs energy flow within solid materials and is described by Fourier's Law, with heat flux proportional to the temperature gradient. The following differential equation describes heat conduction in the bridge deck:

$$\rho C_p \left(\frac{\partial T}{\partial t}\right) + \nabla \cdot \mathrm{q} = \mathrm{Qq} = -\mathrm{k}\nabla\mathrm{T} \tag{1}$$

where ρ is the density (kg/m^3), C_p is the heat capacity at constant pressure (J/(kg·K)), T is the absolute temperature (K), $\frac{\partial}{\partial t}$ is the time derivatives operator, q is the conductive heat flux vector (W/m^2), Q is the heat source (or sink) (W/m^3), k is the thermal conductivity coefficient (W/m·K), and ∇T is the temperature gradient. For completely insulated surfaces of the bridge deck, the heat flux is equal to zero (a Neumann boundary condition) and is described as follows:

$$q = -k\nabla T = 0 \tag{2}$$

Convective heat loss at the top and bottom deck surfaces was modeled based on Newton's law of cooling, considering ambient air temperatures and wind effects through convective heat transfer coefficients. Heat transfer due to convection on an exposed surface is described as:

$$-n \cdot q = h \cdot (T_{ext} - T) \quad (3)$$

where n is the normal vector on the boundary, h is the convective heat transfer coefficient (W/m^2·K), T is the surface temperature (K), and T_{ext} is the external temperature.

Additionally, both thermal radiation and solar radiation inputs were included. Heat transfer due to radiation is governed by two equations describing the effects of thermal radiation (Equation 4) and solar radiation (Equation 5):

$$-n \cdot q = \varepsilon\sigma(T_{ext}^4 - T_s^4) \quad (4)$$

$$-n \cdot q = \propto I \quad (5)$$

where ε is the surface emissivity, σ is the Stefan-Boltzmann constant (a predefined physical constant, 5.67×10^{-8} (W·m^2/K^4), $\propto$ is the absorptivity coefficient, and I is the direct radiation incident to a perpendicular surface (W/m^2). These combined heat transfer pathways helped understand the data collection process to input the required values in numerical simulations.

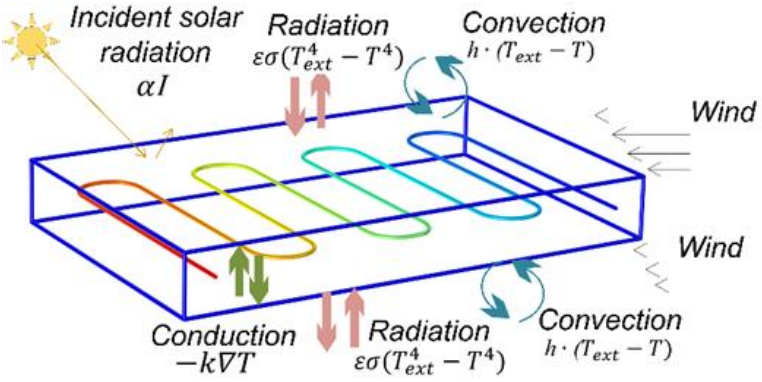


Figure 1: Heat transfer mechanisms in bridge deck (Turner et al., 2024)

Data Collection and Preprocessing

These datasets include ambient and surface temperatures, wind speed, solar radiation, lithological characteristics, thermal ground properties, and ground temperatures. By extracting meaningful features from these datasets, this step aims to provide the necessary inputs for numerical simulations and ML model development. The preprocessing steps ensure data consistency, spatial alignment, and physical relevance, key requirements for building accurate, generalizable models that can evaluate the technical and economic viability of geothermal deicing systems across diverse regions of the state.

Bridge location data was collected from MDT (MDT, 2022). Figure 2(a) shows the geospatial distribution of bridge structures overlaid with major state and federal highways. Data for the electric transmission line locations was obtained from Homeland Infrastructure Foundation-Level Data (HIFLD, 2022). Figure 2(b) shows the locations of electric transmission lines in Montana. Although geothermal deicing systems primarily rely on subsurface heat, they may require electrical components for pumping, control systems, or hybrid integration with solar or grid power. Therefore, the availability and proximity of electrical infrastructure can influence installation feasibility. Proximity to these lines can significantly reduce the cost and complexity of integrating monitoring sensors, programmable thermostats, and auxiliary heating components in a geothermal deicing system.

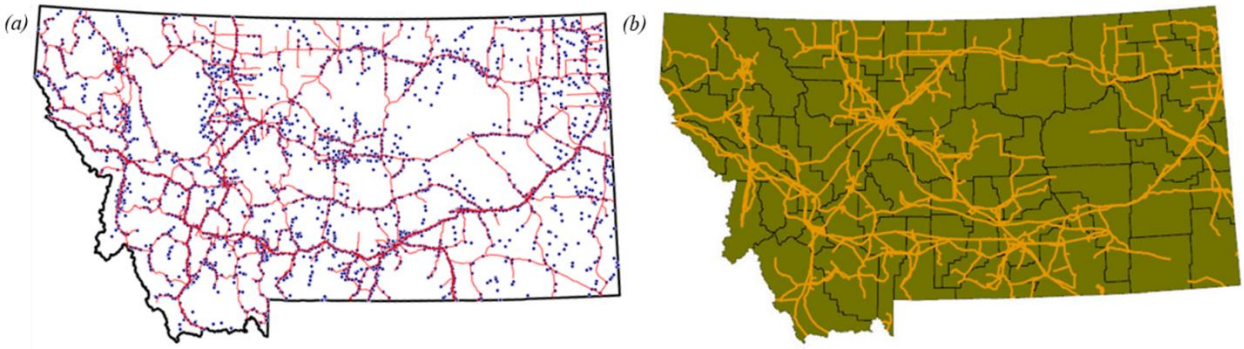


Figure 21: (a) Map of bridges and major roads, and (b) electric transmission lines locations in Montana

Meteorological Data

RWIS stations provide detailed weather information which can be used for winter road and bridge maintenance (Al-Kaisy & Ewan 2017). The 73 stations in Montana include an air temperature and humidity sensor, wind speed and direction sensor, in-pavement temperature sensor, subsurface temperature sensor, precipitation sensor, and camera.

Ambient Temperature: Figure 3(a) shows the locations of the 73 RWIS stations in Montana. Figure 3(b) shows the distribution histogram of average ambient temperature for Montana. Temperature data were recorded at 10-minute intervals from 2016 to 2019 at 24 locations across the state. For each 12-hour period, the average temperature was calculated as the mean of all 10-minute readings, while the maximum and minimum represent the highest and lowest values within that same interval. These 12-hour average, maximum, and minimum temperatures were used for analysis. Figure 3(c) presents the time series of ambient temperatures for site ID 150000, located west of Montana, including the average, maximum, and minimum temperature values. The plot shows the maximum, average and minimum ambient temperature values for 2016-2019. The data

show that a bridge deck deicing system should be designed for the months of November through March because they have the lowest average temperatures, as low as −10°C.

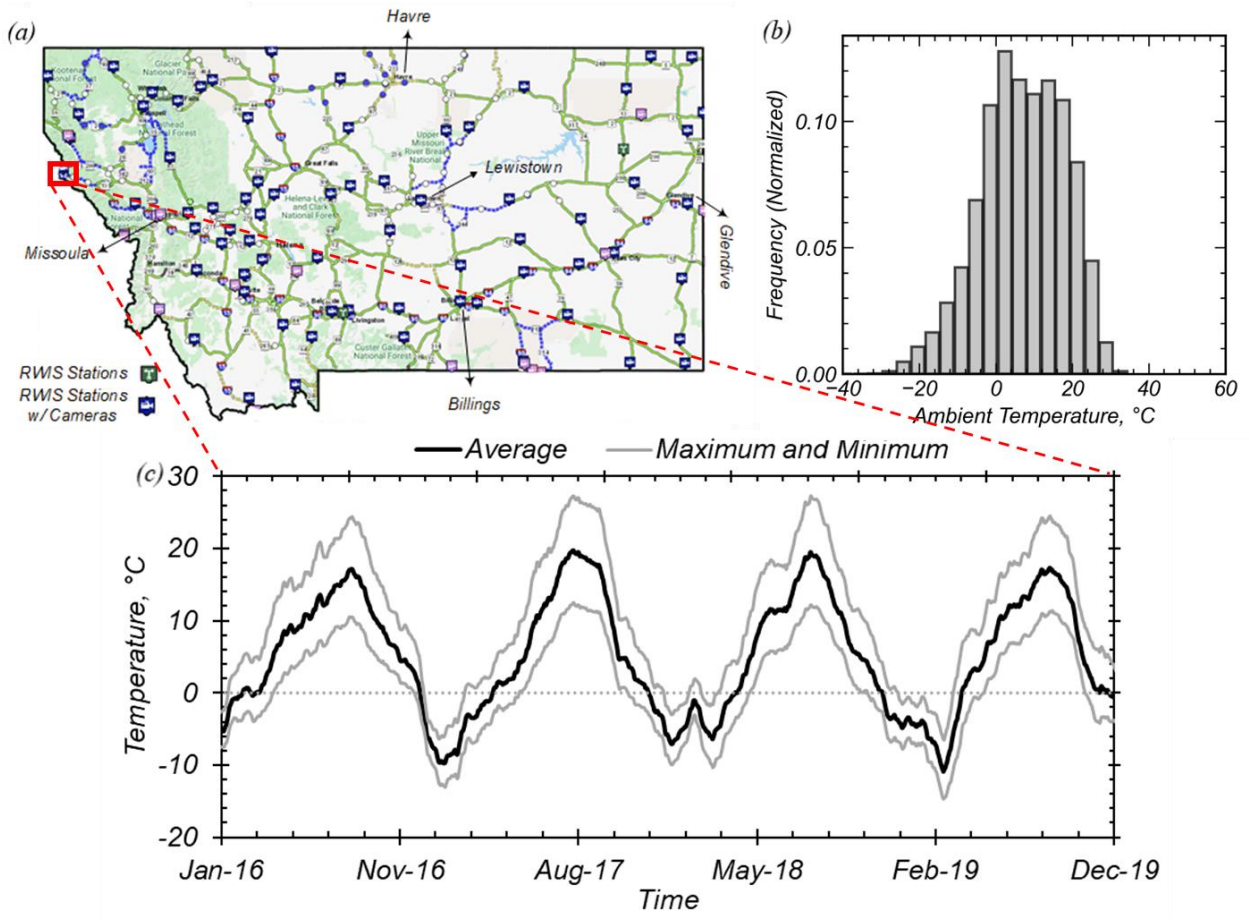


Figure 3: (a) Locations of MDT RWIS sites (map source: https://roadreport.mdt.gov/), (b) average ambient temperature distribution histogram for Montana, and (c) time series of ambient temperatures for 2016–2019 (site ID 150000)

Figure 4 shows the spatial distribution of the average annual ambient temperature across the state of Montana, generated using ordinary kriging interpolation in ArcGIS Pro. The temperature values range from approximately 3.6°C to 8.6°C, with distinct spatial patterns evident across the state. Warmer regions are predominantly located in the central, eastern, and some portions of northern Montana, reflecting lower elevations and continental climatic influences. In

contrast, cooler areas are concentrated in the southwestern mountainous regions, where higher elevations and orographic effects contribute to reduced annual temperatures. The kriging approach allowed for the estimation of temperature values in unsampled areas, resulting in a continuous heat map that captures both broad regional trends and localized variability.

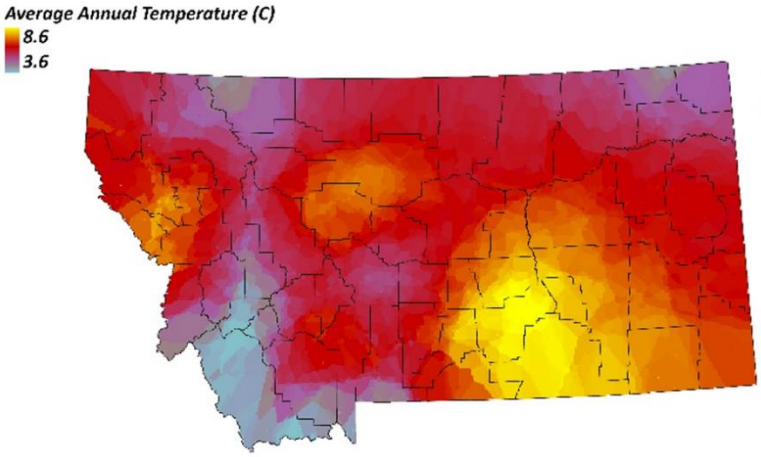


Figure 4: Heat map of average annual temperature in Montana using Kriging interpolation

Wind Speed: Figure 5 presents the statistical distribution and spatial variability of wind speed across Montana, based on measurements from 26 monitoring stations. Figure 5(a) displays the normalized frequency histogram of recorded wind speeds. The distribution exhibits a pronounced positive skew, with the majority of wind speeds concentrated between approximately 5 km/h and 20 km/h, and a peak frequency occurring near 10 km/h. The tail of the distribution extends toward higher wind speeds, with occasional events reaching up to 50–60 km/h, although these occurrences are relatively rare. This distribution shows that moderate wind conditions are common across the state, with extreme wind events being infrequent. Figure 5(b) shows the spatial distribution of the coefficient of variation (COV) of wind speed across the 26 station locations. The coefficient of variation, defined as:

$$COV = \frac{\sigma}{\mu} \tag{6}$$

where σ is the standard deviation and μ is the mean wind speed. This provides a normalized measure of variability relative to the mean value. Spatially, the COV values vary from approximately 0.45 to 0.82 across the state. Higher COV values, indicated by yellow and green markers, suggest regions where wind speed is highly variable relative to the mean, whereas lower COV values (purple hues) represent areas with more consistent wind conditions. Notably, some western and southern parts of Montana show more variability in wind speeds. Higher and more variable wind speeds can significantly increase convective heat loss from the bridge surface during winter conditions, leading to lower surface temperatures. As a result, geothermal systems would require additional energy input to maintain the bridge deck above freezing. Both the average wind speeds and their variability are therefore important for predicting operational efficiency of geothermal deicing systems across Montana.

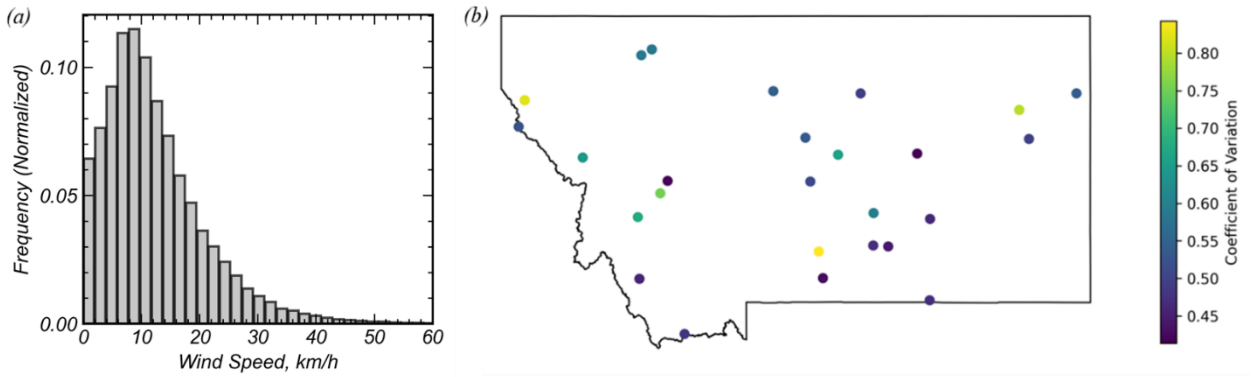


Figure 5: (a) Frequency distribution of wind speeds in Montana, and (b) spatial distribution of the coefficient of variation of wind speeds across Montana

Solar Radiation: Figure 6 shows the normalized frequency distribution of shortwave surface downward solar radiation under all-sky conditions, representing the solar energy incident

on bridge deck surfaces. The distribution is positively skewed, with a pronounced peak occurring between approximately 75 and 125 W/m². This indicates that relatively low to moderate solar radiation levels are most common across the study area. Beyond the peak, the frequency gradually decreases as solar radiation increases, with substantial occurrences observed up to approximately 300 W/m². All-sky solar radiation was plotted, as it accounts for the combined effects of clear, partly cloudy, and overcast conditions, thus providing a realistic representation of the actual solar energy reaching the bridge surface. The observed trend suggests that, for most of the time, bridge decks are subjected to solar radiations ranging from 75 to 300 W/m².

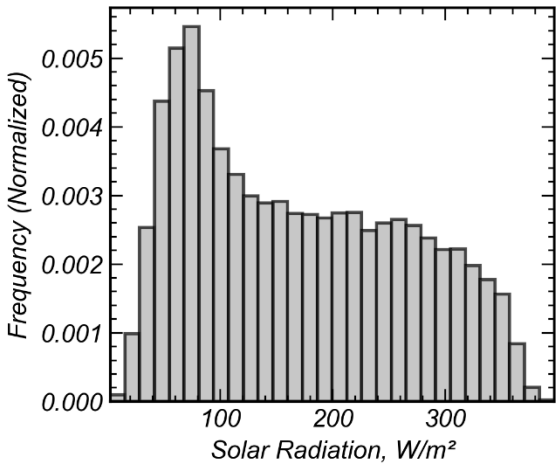


Figure 6: Frequency distribution of shortwave solar radiation in Montana

Ground Temperature

Figure 7 provides an overview of the ground temperature characteristics across Montana, based on data collected from over 1,000 wells statewide. Figure 7(a) presents the normalized frequency distribution of ground temperatures. The majority of ground temperatures cluster between approximately 3.6°C and 20°C, consistent with the expectation that shallow ground temperatures broadly reflect the average annual ambient temperature. However, a distinct

secondary peak is observed near 50°C, which can be attributed to the presence of geothermal anomalies, specifically hot springs, that are distributed across various regions in Montana. This bimodal distribution highlights the unique geothermal character of the state. Figure 7(b) illustrates the relationship between ground temperature and depth. The scatter plot reveals that ground temperature appears largely independent of depth within the observed range, with similar temperatures recorded from shallow to deeper wells (up to 150 meters). This finding suggests that localized geothermal conditions, rather than thermal gradients with depth, primarily control ground temperature variations in Montana. Figure 7(c) maps the spatial distribution of ground temperatures, with red dots representing well locations. The kriging interpolation reveals that most of the state exhibits ground temperatures ranging from 3.6°C to about 20°C, while concentrated hotspots with elevated temperatures up to 49.5°C are evident, particularly in southwestern and south-central Montana. These localized zones correspond to areas of geothermal activity, reinforcing the influence of natural hot springs on regional ground temperature variability. The wide spatial coverage and variability in ground temperatures captured here are important to define the capacity for geothermal resource assessments across Montana.

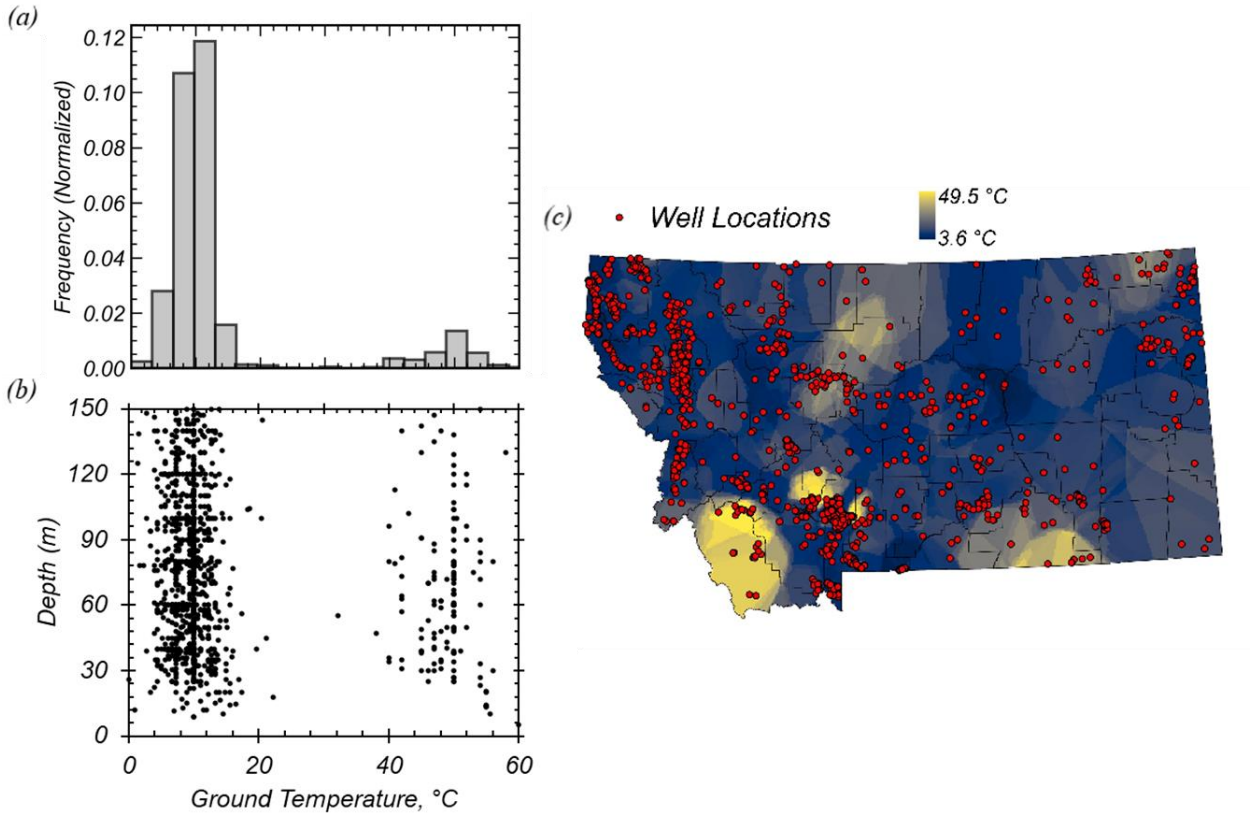


Figure 7: Ground temperature characteristics across Montana: (a) normalized frequency distribution of ground temperatures, (b) ground temperature versus depth, and (c) spatial distribution of ground temperatures and well locations

Ground Properties

Figure 8 shows the spatial distribution of soil thermal properties across Montana, derived from the United States Geological Survey (USGS) soil classification system (Robertson, 1988). The values of thermal conductivity and thermal capacity were interpolated over the state. Figure 8(a) presents the variation in thermal conductivity (W/mK), a measure of the soil's ability to conduct heat. Thermal conductivity values across the state range from approximately 1.0 W/mK to 3.5 W/mK. Higher thermal conductivities are observed in the mountainous and rocky regions of north-western Montana, and most parts of central Montana, indicated by darker brown hues,

whereas lower thermal conductivity values are more concentrated in the western part of the state. This spatial variability is significant for evaluating the heat transfer efficiency from geothermal systems embedded within different soil types. Figure 8(b) displays the spatial variation of thermal capacity (MJ/m³K), which represents the amount of heat required to change the temperature of a unit volume of soil by one degree Kelvin. Thermal capacity values range from approximately 2.0 to 2.9 MJ/m³K. Generally, higher thermal capacities are associated with regions containing higher moisture content or denser soils, as indicated in the plot along the mountainous belts. And lower thermal capacities are observed in the drier and less dense soils across the eastern plains.

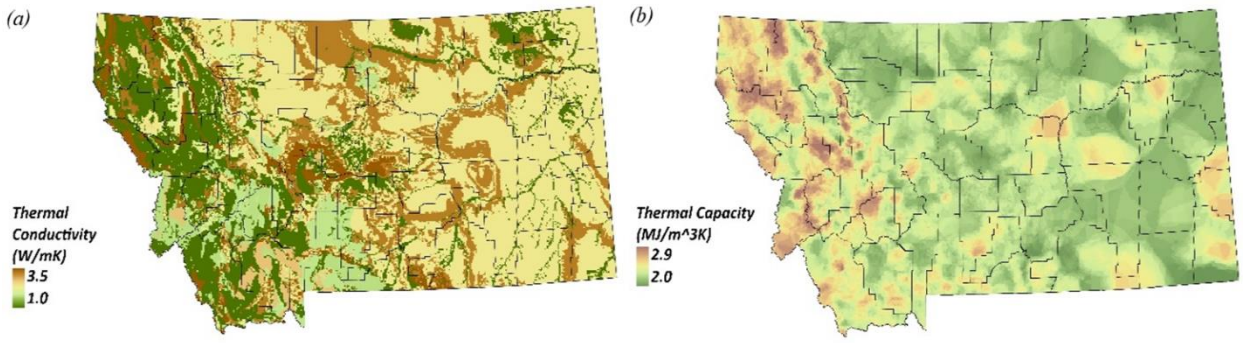


Figure 8: Soil thermal properties across Montana: (a) spatial distribution of thermal conductivity based on USGS soil classification, and (b) spatial distribution of thermal capacity based on USGS soil classification

Numerical Model Development

A numerical model was constructed in COMSOL Multiphysics to evaluate the effect of various parameters of a bridge deck deicing system. Concrete temperature and top surface strain results from experiments conducted by Turner et al. (2024) were used to validate the numerical model. Once constructed and validated, the model was used to generate the data required for training machine learning models aimed at predicting bridge deck surface temperature and

evaluating the performance of geothermal heating systems under varied environmental and design conditions.

Overview of the experiments:

A model-scale bridge deck with embedded heat exchanger tubing was constructed and tested in the Cold Hydrodynamics Chamber (CHC) of Montana State University's Subzero Research Laboratory (Turner et al. 2024a; Turner et al. 2024b). The goal of the experiments was to collect detailed surface and internal temperature measurements under varying environmental conditions in order to validate a numerical model developed to simulate geothermal bridge deck heating performance. Figure 9 illustrates the experimental model configuration used to validate the numerical simulations of a geothermal bridge deck deicing system. Figure 9(a) presents a plan view of the model, showing the embedded layout of the heat exchanger tubing and the distribution of temperature and strain sensors (Turner et al. 2024). Figure 9(b) shows a sectional view, highlighting the cross-sectional arrangement of the tubing and sensor placements relative to the bridge deck geometry. The model-scale bridge deck was constructed to replicate realistic thermal and structural behavior while maintaining manageable laboratory dimensions. The tubing system, composed of cross-linked polyethylene (PEX) pipes with a 12.7 mm diameter, was embedded with 20 cm center-to-center spacing, simulating typical installation practices in full-scale geothermal systems. The tubing was attached beneath the top layer of steel reinforcement to preserve concrete cover requirements, which is critical for ensuring long-term durability against environmental exposure. The sides of the model were insulated to promote a one-dimensional heat transfer condition through the top and bottom surfaces, isolating the effects of geothermal heating and environmental interactions. The use of insulation along the sides ensured that the experimental

results focused on conditions representative of the interior sections of a full-scale bridge deck, where heat dissipation to ambient air would be minimal. The experimental setup incorporated 30 Type-T thermocouples distributed throughout the deck to measure temperature profiles. This detailed sensor network and thermal boundary configuration were essential for capturing the heat transfer behaviors needed for numerical model validation. The experimental measurements formed the basis for calibrating the numerical simulations developed in COMSOL Multiphysics, ensuring that the temperature evolution under simulated Montana winter conditions could be accurately reproduced.

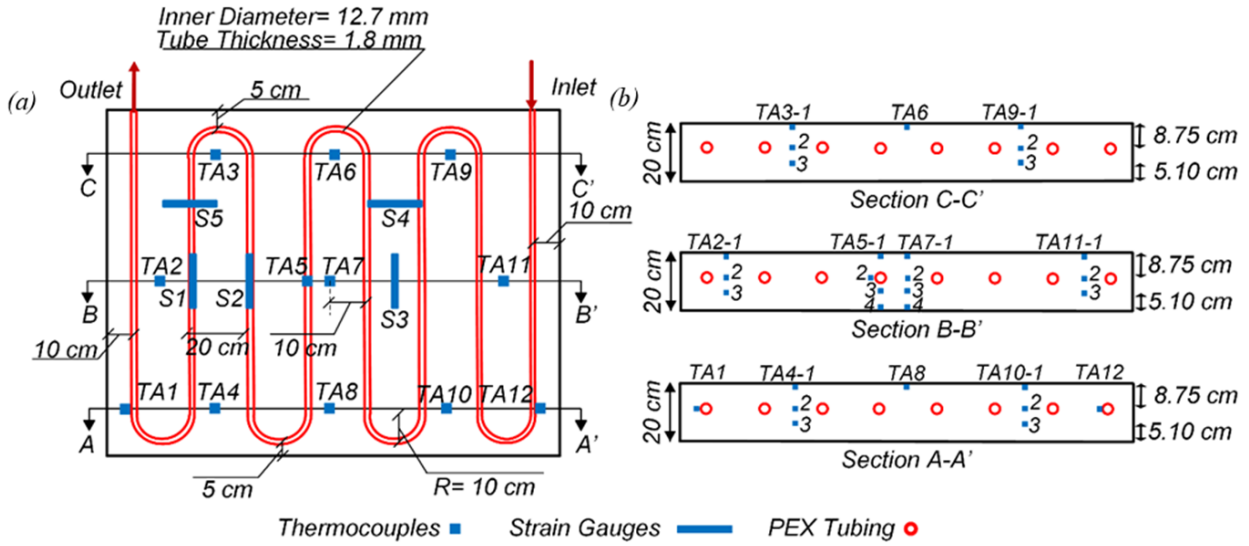


Figure 9: Experimental model configuration with sensor locations: (a) plan view; and (b) section views (Turner et al., 2024)

Overview of Numerical Model

The geothermal bridge deck deicing system was simulated using a 3D numerical model developed in COMSOL Multiphysics. The heat transfer mechanisms previously described, including conduction, convection, and radiation, were incorporated into the numerical model. These mechanisms govern the energy exchange between the bridge deck and its environment and

were implemented using established physical laws as detailed in the earlier section. Their inclusion enabled the model to accurately capture the thermal behavior of the bridge deck under varying cold-weather conditions.

The 3D numerical model replicates the experimental bridge deck dimensions and material characteristics, shown in figure 10(a). The embedded heat exchanger pipes were modeled using the non-isothermal pipe flow module, treating fluid flow as one-dimensional while allowing for coupling with surrounding solid conduction. Pipe-wall heat transfer, fluid velocity, pressure losses, and frictional effects were incorporated to accurately represent the thermal behavior of the circulating glycol-water mixture. The boundary conditions were assigned to simulate experimental conditions. The sides of the bridge deck were thermally insulated to minimize lateral heat loss, while the top and bottom faces were exposed to convective and radiative boundary conditions. Solar radiation was applied as a surface heat flux input, enabling simulation of daytime heating effects under varying ambient conditions.

The finite element mesh of the bridge deck, shown in figure 10(b), was generated to balance computational efficiency and numerical accuracy. Material properties, including thermal conductivity, specific heat capacity, density, and coefficients of thermal expansion, were assigned based on standard concrete values and calibrated during model validation. To validate the numerical model, the input parameters, shown in table 1, from the experimental setup were transferred into the COMSOL environment.

Table 1: Material properties of the numerical model

Parameter	***Value***
Bridge Deck Dimensions	
Length (m)	1.60
Width (m)	1.00
Height (cm)	20.00
Depth of circulation pipes (cm)	8.75

Circulation Fluid	
Flow rate (L/m)	5.50
Dyncamic viscosity (mPa·s)	4.80
Thermal conductivity (W/m·k)	0.40
Specific heat capacity (J/kg·k)	3538.00
Density (kg/m^3)	1070.00
Concrete	
Thermal conductivity (W/m·k)	1.00
Specific heat capacity (J/kg·k)	880.00
Density (Kg/m^3)	2400.00
Coefficient of thermal expansion (με/°C)	10.00
Surface emissivity	0.85
Absorptivity coefficient	0.58
Concrete Zones	
Top height (cm)	9.00
Bottom height (cm)	6.67
Top thermal conductivity (W/m.k)	1.60
Top specific heat capacity (J/kg.k)	874.37
Top density (Kg/m^3)	2475.71
Bottom thermal conductivity (W/m.k)	2.16
Bottom specific heat capacity (J/kg.k)	869.24
Bottom density (Kg/m^3)	2544.80

Overall, the numerical model was designed to simulate the thermal and mechanical behavior of a geothermal bridge deck system under representative Montana winter scenarios. The detailed coupling of heat transfer, fluid flow, and structural response provides a robust platform for evaluating system effectiveness for feasibility analysis of geothermal systems.

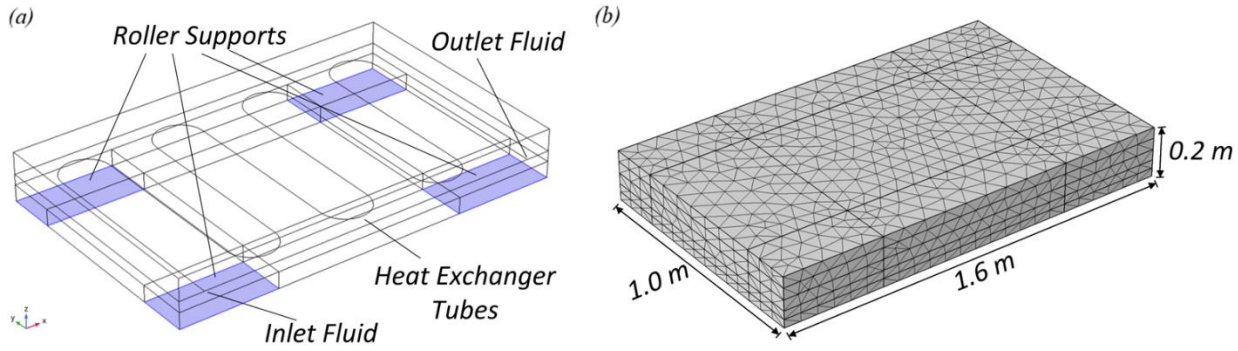


Figure 10: Overview of the numerical model: (a) numerical model configuration, and (b) meshed model in COMSOL Multiphysics (Turner et al., 2024)

Model Validation:

The developed numerical model was validated by comparing its predictions against experimental results obtained from two distinct weather scenarios designed to assess system performance (Turner et al., 2024). Figure 11 presents the comparison between simulated and measured concrete temperatures for (a) a synthetic scenario isolating temperature and solar radiation effects and (b) a daily fluctuation scenario simulating typical winter diurnal cycles. In the synthetic scenario (Figure 11a), the bridge deck was subjected to four consecutive 24-hour stages, each characterized by different ambient temperatures (ranging from −10°C to −20°C) and varying solar radiation intensities (from 0 to 490 W/m²) following an initial stabilization at 10°C. In contrast, the daily fluctuation scenario (Figure 11b) represented a repeating 24-hour cycle with ambient temperatures increasing from −5°C to 10°C over an 8-hour period, accompanied by a ramp-up and ramp-down in solar radiation intensity over shorter intervals. Prior to initiating the cyclic changes, the concrete was stabilized at an ambient temperature of −5°C. For both scenarios, temperature measurements from thermocouples located at various depths and surfaces (TA8, TA11-2, TA10-3, and TA7-4) were used for model validation.

The results from the synthetic scenario (Figure 11c) demonstrated close agreement between experimental observations and numerical predictions during Stages 1 and 4, where solar radiation was absent. However, during Stages 2 and 3, when solar radiation was introduced, the numerical model tended to slightly underestimate surface temperatures compared to experimental data, except at the bottom surface (TA7-4), where agreement remained consistent. A temporary malfunction in the solar simulator during the early part of Stage 3 led to irregularities in the experimental surface temperature measurements, though these deviations were corrected later in the stage. Excluding the anomaly caused by the simulator malfunction, the maximum deviation

between modeled and measured temperatures was approximately 1.5°C. These discrepancies can largely be attributed to the challenges in accurately replicating the spatial non-uniformity of solar radiation distribution across the bridge deck in the numerical model, due to the centralized positioning of the solar simulator.

In the daily fluctuation scenario (Figure 11d), the model demonstrated good agreement with experimental results throughout the testing period, particularly at the top surface (TA8). Minor deviations of up to 1.5°C were noted for internal concrete temperatures (TA11-2 and TA10-3) during Stages 1 and 3, and for the bottom surface (TA7-4) during Stage 2. These minor discrepancies are also attributed to the complexities associated with accurately modeling solar radiation effects. Nevertheless, the overall temperature trends, magnitudes, and thermal response captured by the numerical model strongly align with the experimental observations, supporting the model's validity for subsequent parametric studies and performance evaluations under Montana winter conditions.

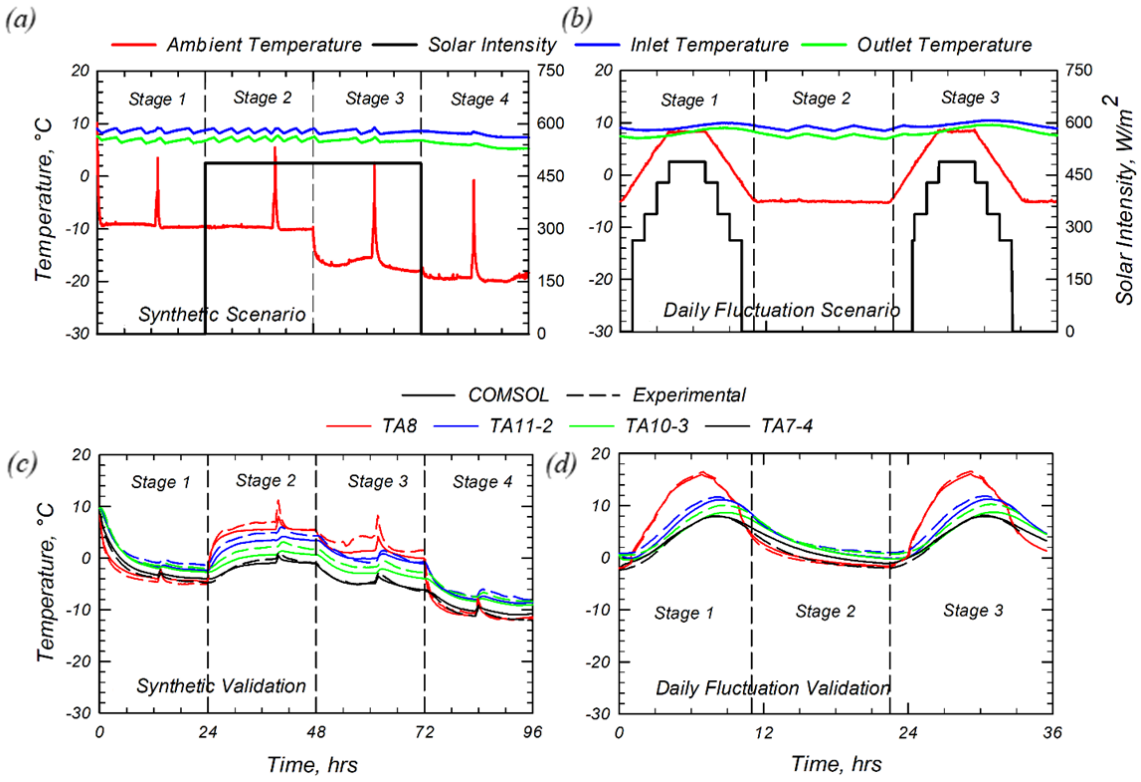


Figure 11: (a) synthetic scenario test plan, (b) daily fluctuation scenario test plan, (c) synthetic scenario validation, and (d) daily fluctuation scenario validation

Parametric Study

Following model validation, a comprehensive parametric study was conducted to investigate the influence of key design and environmental variables on the thermal behavior of the geothermal bridge deck deicing system. The goal of this study was to identify the sensitivity of surface temperature response to changes in input parameters and to quantify their individual and combined impacts on system performance. These insights are critical for informing optimal system design, guiding operational strategies, and supporting the development of data-driven predictive models in Chapter 3.

The parameters explored in this study include ambient temperature, wind speed, solar radiation, inlet fluid temperature, fluid flow rate, tube spacing, and bridge deck length. For the parametric studies, a baseline model was established, and each parameter was varied independently while keeping all other conditions constant. This approach enabled an isolated evaluation of the thermal response associated with each parameter. The properties of the baseline model are presented in table 2.

Table 2: Properties of baseline model for parametric studies

Parameter	***Value***
Ambient Temperature (°C)	-10
Wind Speed (km/h)	10
Solar Radiation (W/m^2)	160
Inlet Fluid Temperature (°C)	10
Fluid Flowrate (L/min)	10
Tube Spacing (cm)	20
Bridge Deck Length (m)	1.6

Ambient Temperature

Ambient air temperature plays a key role in controlling convective and radiative heat losses from the bridge surface. To evaluate its influence, simulations were performed at ambient temperatures of –15 °C, –10 °C, –5 °C, and 0 °C, with other parameters held constant in the baseline model. The initial surface temperature was set equal to the ambient temperature to reflect thermal equilibrium at startup. As shown in figure 12, colder ambient conditions significantly reduce surface warming. At –15 °C, the surface temperature remains below freezing, reaching a maximum of only –4.5 °C after 24 hours. At –10 °C, it takes about 10 hours to reach 0 °C and stabilizes around 2 °C. Under –5 °C, freezing is reached in 5 hours, with a final temperature of ~4.5 °C. At 0 °C, the surface surpasses the freezing point within 2 hours and stabilizes near 7.5 °C. These results highlight the sensitivity of geothermal de-icing systems to ambient temperature.

Colder air increases the thermal gradient and accelerates heat loss, potentially preventing effective de-icing. Design strategies must therefore consider regional climate conditions to ensure reliable system performance under extreme cold.

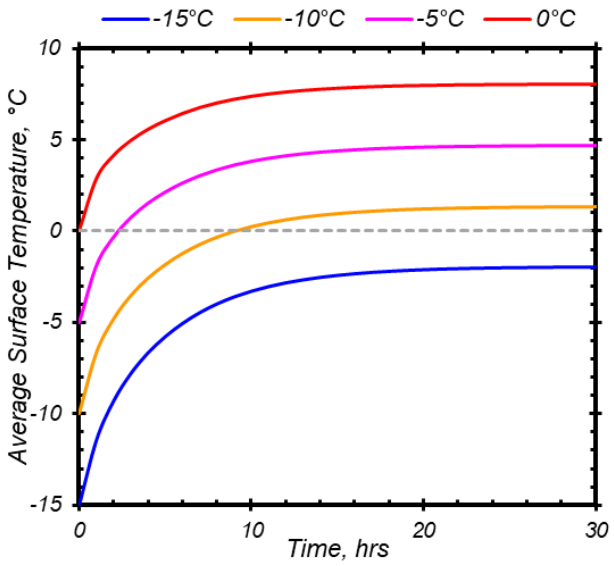


Figure 12: Influence of ambient temperature on surface temperature and heating time

Wind Speed

Wind speed influences surface heat transfer primarily by enhancing convective cooling, thereby accelerating thermal energy loss from the bridge deck to the atmosphere. Simulations were conducted for wind speeds of 0, 10, and 40 km/h, covering typical to extreme winter wind conditions in Montana. The initial bridge surface temperature was set at –10 °C. As shown in figure 13, increased wind speed significantly reduces surface warming. Without wind, the surface reaches 0 °C in approximately 5 hours and stabilizes near 8 °C after 24 hours. At 10 km/h, the surface reaches the freezing point in about 9 hours and levels off at ~3.5 °C. However, at 40 km/h, the surface temperature fails to exceed 0 °C, stabilizing near –4.5 °C, indicating ineffective de-icing. These results highlight that higher wind speeds markedly increase convective heat transfer

coefficients, delaying the time to reach critical de-icing temperatures and lowering the equilibrium surface temperature. This underscores the need to consider wind exposure in the thermal design and operational control of bridge deck de-icing systems.

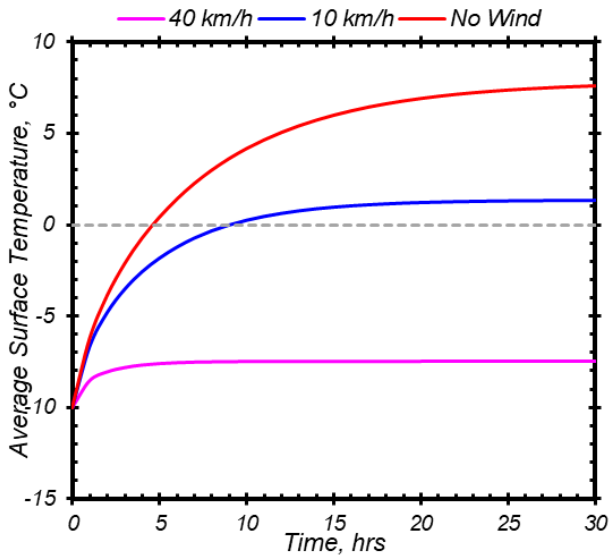


Figure 13: Influence of wind speed on surface temperature response

Solar Radiation

Figure 14 illustrates the influence of solar radiation intensity on bridge surface temperature. The simulations consider three solar intensity levels—0 W/m² (no solar), 160 W/m² (partly cloudy), and 360 W/m² (clear sky)—representing realistic winter solar conditions in Montana. The initial surface temperature is set to –10 °C to reflect typical cold-season conditions. The results show a strong correlation between solar input and surface warming. Under no solar radiation, the surface temperature remains below freezing and reaches a maximum of approximately –1.5 °C after 24 hours, failing to de-ice the bridge deck. At 160 W/m², the surface temperature crosses 0 °C after roughly 8 hours and stabilizes at around 3.5 °C. Under 360 W/m², the deck reaches 0 °C in approximately 4 hours and eventually stabilizes at nearly 6.5 °C. These findings highlight that

increased solar radiation significantly reduces the time to reach the freezing point and enhances the maximum surface temperature. Consequently, solar gain can markedly reduce the energy burden on the geothermal loop, underscoring its value in optimizing hybrid geothermal-solar deicing systems for cold region infrastructure.

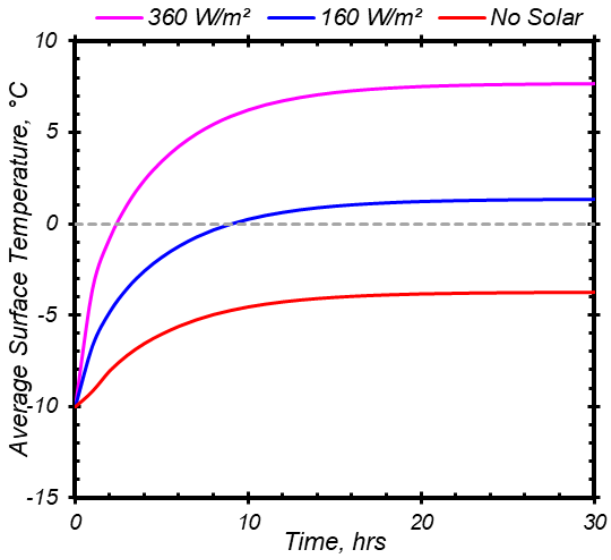


Figure 14: Influence of solar radiation intensity on bridge surface temperature

Inlet Temperature

The inlet temperature of the circulating fluid plays a critical role in determining the thermal energy delivered to the concrete slab. Figure 15 presents simulation results for inlet fluid temperatures of 10 °C and 50 °C, representing the range of feasible geothermal ground temperatures in Montana. The initial surface temperature is assumed to be –10 °C, representative of typical winter conditions in the region. As shown in figure 15, higher inlet fluid temperatures significantly improve de-icing performance. With a 50 °C inlet temperature—characteristic of geothermal hot spring zones—the bridge surface temperature crosses the freezing threshold (0 °C) in under 2 hours and stabilizes at approximately 18 °C after 24 hours. In contrast, with a 10 °C

inlet temperature, the surface temperature requires approximately 6 hours to reach 0 °C and stabilizes at around 6 °C. This highlights the strong influence of inlet temperature on both the rate of de-icing and the final thermal condition of the bridge deck, emphasizing the potential benefits of utilizing higher geothermal gradients where available.

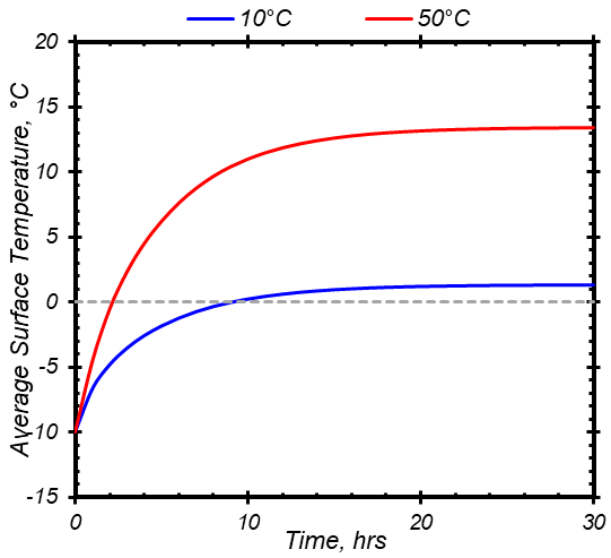


Figure 15: Surface temperature response for different inlet fluid temperatures

Flow Rate

The flow rate controls the rate at which thermal energy is delivered to the bridge deck via circulating fluid. Simulations were conducted for flow rates of 10 L/min and 25 L/min, with an initial surface temperature of –10 °C and other conditions held constant. As shown in figure 16, increasing the flow rate from 10 L/min to 25 L/min has a negligible impact on surface temperature dynamics. In both cases, the surface temperature reaches 0 °C in approximately 8 hours and stabilizes around 1.5 °C after 15 hours. This suggests that, within this flow range, thermal transport is not a limiting factor in system performance. However, it is worth noting that flow rate may have a more pronounced effect at lower values, where thermal delivery becomes insufficient to

overcome surface heat losses. Therefore, while increasing flow beyond moderate rates yields diminishing returns, ensuring a minimum threshold flow rate remains critical for effective de-icing.

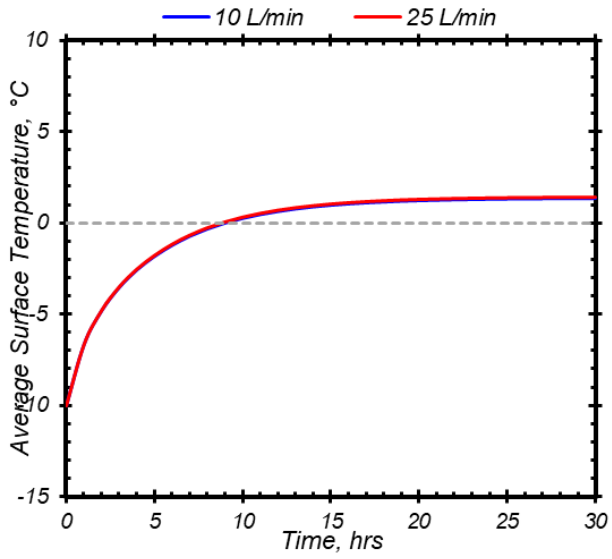


Figure 16: Influence of fluid flow rate on surface temperature and heating efficiency

Tube Spacing

Tube spacing controls the uniformity and extent of thermal distribution within the bridge deck. Wider spacing reduces material costs but may lead to localized cold zones. Figure 17 shows the results for 20 cm and 30 cm of tube spacing. As shown in the figure, narrower spacing improves surface temperature and reduces the time to de-ice. However, the effect is very minimal on the average bridge deck surface temperature. But, a spacing of 20 cm may provide more uniform temperature distributions throughout the bridge deck.

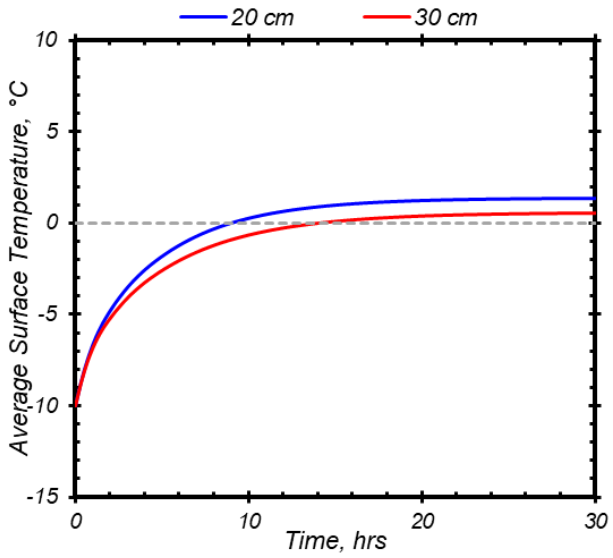


Figure 17: Impact of tube spacing on surface temperature distribution

Bridge Length

Bridge length can influence heat loss due to extended piping and increased surface area exposed to ambient conditions. To evaluate this effect, simulations were performed for bridge lengths of 1.6 m, 3.2 m, and 4.8 m, with identical inlet temperatures, flow rates, and tubing densities. The initial surface temperature was set at –10 °C for all cases. As shown in figure 18, surface temperature responses were nearly identical across all bridge lengths. The time to reach 0 °C was approximately 8 hours for each case, and all simulations stabilized near 1.5 °C after 15 hours. This uniformity is attributed to the same tubing density and adequately high flow rate, which maintained sufficient thermal energy delivery across the full bridge span. These results suggest that, under proper design conditions, bridge length within this tested range does not significantly affect surface temperature performance or de-icing efficiency.

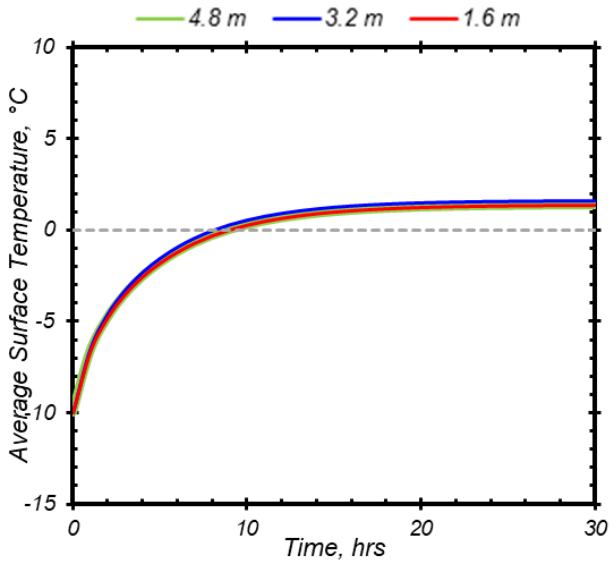


Figure 18: Surface temperature profiles for varying bridge lengths

Effect of Solar, Inlet Temperature, and Tubing

Figure 19 illustrates the combined effect of inlet fluid temperature and solar radiation on bridge deck surface temperature. Simulations were conducted for inlet temperatures of 10 °C and 50 °C, both with and without solar radiation (360 W/m²). A reference case without tubing (passive solar only) was also included. The initial surface temperature was set at –5 °C for all scenarios. In the absence of tubing, solar radiation alone raises the surface temperature to ~10 °C over 24 hours, while no solar input leaves the surface at ~–5 °C, indicating no warming. With a 10 °C inlet and no solar radiation, the surface reaches 0 °C in ~7.5 hours and stabilizes at ~2.5 °C. When solar is added, the temperature reaches 0 °C in ~4 hours and stabilizes near 11 °C. For the 50 °C inlet case, the surface reaches 0 °C in under 2 hours. Without solar, it stabilizes at ~17.5 °C, and with solar, it rises to ~22.5 °C. These results demonstrate that both inlet temperature and solar radiation significantly affect system performance, with higher inlet temperatures and solar input reducing

time to de-ice and increasing the final surface temperature. Their combined use offers substantial enhancement in thermal efficiency and de-icing reliability.

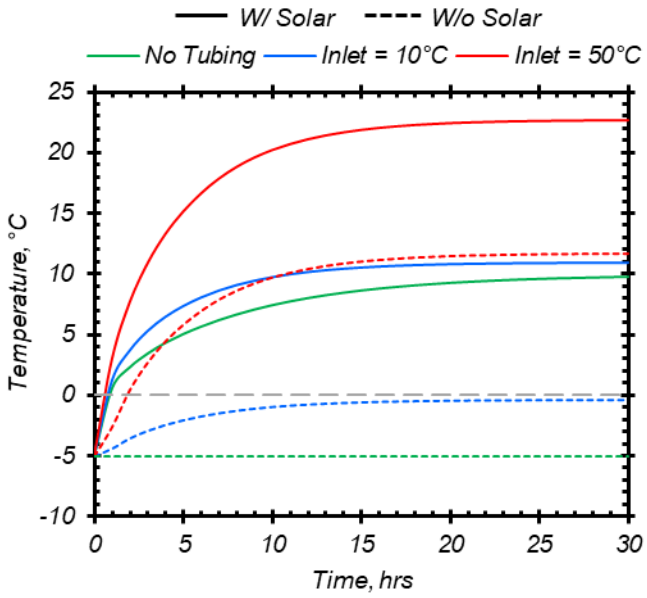


Figure 19: Bridge deck surface temperature with and without solar radiation, for different inlet temperatures

CHAPTER THREE

MACHINE LEARNING MODEL DEVELOPMENT

Introduction

This chapter will be submitted as a journal paper in 2025. The validated numerical model developed in Chapter 2 successfully captured the thermal behavior of bridge decks subjected to geothermal heating under varied environmental and design conditions. While these simulations provide high accuracy, their computational cost and time-intensive nature pose limitations for practical, large-scale deployment across hundreds of bridges in Montana. To address this challenge, this chapter introduces a machine learning (ML)-based framework designed to deliver rapid, accurate, and scalable predictions of bridge surface temperature and deicing performance under different environmental conditions.

The primary objective of this chapter is to develop supervised machine learning models that learn from numerical simulations and emulate the thermal behavior of geothermal bridge deck systems. These models can then be used to evaluate system performance in real time without requiring repetitive and computationally expensive simulations. The ML workflow encompasses six structured steps, from feature selection and data generation to model evaluation and interpretation.

Prediction Model Development Framework

The prediction model development framework begins with the generation of a structured dataset using the validated COMSOL Multiphysics model. Input features include environmental and design parameters, while target outputs include surface temperature and system response

metrics. The generated dataset is used to train machine learning algorithms that can make predictions for a wide range of conditions. This framework enables automated, rapid evaluations once the model is trained.

Machine Learning Model Development Process

Figure 20 summarizes the machine learning model development process for training and evaluating the prediction models. For this study, the machine learning development was carried out in six steps. The first step, feature selection, involved identifying the most physically relevant and influential parameters affecting bridge deck surface temperature. This was accomplished through detailed parametric studies conducted using the validated numerical model (Chapter 2). Each parameter was systematically varied, and its impact on the thermal response was evaluated. Based on these analyses, a final set of seven features was selected: ambient temperature, wind speed, solar radiation, inlet fluid temperature, flow rate, tube spacing, and bridge length. These features were chosen to ensure that both environmental variability and design-dependent behaviors were captured in the training dataset. The second step involved generating a comprehensive dataset using COMSOL-based simulations automated through MATLAB LiveLink. More than 2,000 simulations were performed across a structured design space that encompassed combinations of the selected features. The simulations captured surface temperature responses under both "with tubing" and "without tubing" conditions. This dataset formed the foundation for training machine learning models capable of replicating the thermal behavior of geothermal bridge deck systems. In the third step, data splitting and experimental design were applied. The dataset was divided using an 80/20 train-test split, and five-fold cross-validation was implemented to reduce overfitting and ensure robustness. The fourth step focused on model selection and training. Two predictive models

were developed: Model 1, designed to estimate system performance metrics such as stabilized surface temperature, time to reach above 0°C, and time to stabilization; and Model 2, which provided continuous surface temperature predictions at every 0.1-hour interval. Both models used the same input features but differed in output structure. A wide range of supervised learning algorithms were employed for both models, including linear regression, polynomial regression, decision trees, random forests, XGBoost, and fully connected neural networks (FCNN). Each algorithm was trained on the simulation-derived dataset, and model selection was subsequently performed based on lowest cross validation error. In the fifth step, model evaluation was performed using three standard metrics: mean absolute error (MAE), root mean squared error (RMSE), and coefficient of determination (R^2). These metrics allowed for quantitative comparison across different algorithms and configurations. The final step involved sensitivity analysis to further understand model interpretability. A permutation-based approach was used, where each input feature was shuffled independently while observing the resulting increase in prediction error. This analysis revealed that inlet temperature, ambient temperature, wind speed, and solar radiation were the most influential predictors. The findings were consistent with the results from parametric studies.

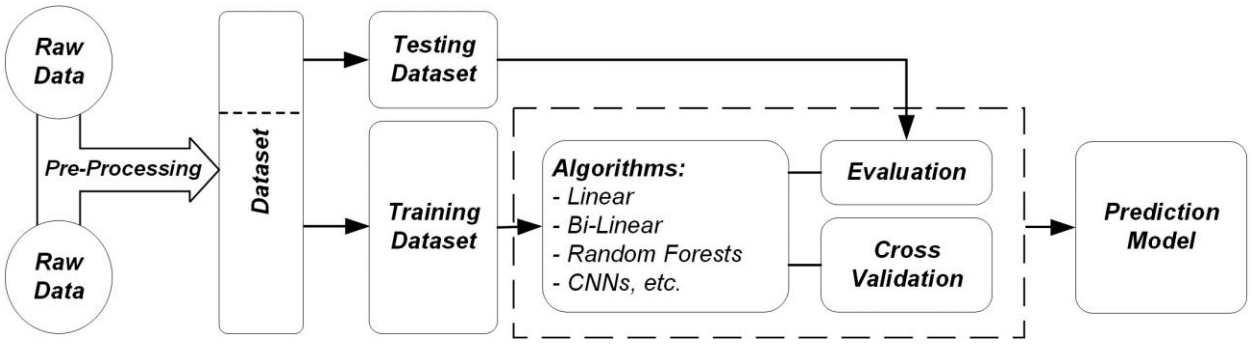


Figure 20: Machine learning model development process

Step 1: Feature Selection

The first step in developing a predictive ML model is identifying the most relevant input features. These features should represent the physical variables that influence surface temperature response and deicing performance. Based on the parametric studies, feature sensitivity, and engineering domain knowledge, ambient temperature (°C), wind speed (km/h), solar radiation (W/m²), inlet fluid temperature (°C), flow rate (L/min), tube spacing (cm), and bridge deck length (m), were selected as input features for the machine learning models. Figure 21 shows the effect of varying each parameter on the bridge deck average surface temperature. A baseline configuration was selected for the sensitivity analysis. Each feature was independently varied while all other parameters were held constant, allowing for the isolated evaluation of its influence on the system's thermal response. The properties of the baseline model are presented in table 3.

Table 3: Properties of baseline model for feature sensitivity

Parameter	***Value***
Ambient Temperature (°C)	-10
Wind Speed (km/h)	10
Solar Radiation (W/m^2)	160
Inlet Fluid Temperature (°C)	20
Fluid Flowrate (L/min)	10
Tube Spacing (cm)	25
Bridge Deck Length (m)	3.2
Initial Temperature (°C)	-10

For each variation, the resulting change in stabilized surface temperature was recorded. As shown in Figure 21, inlet temperature, ambient temperature, wind speed, and solar radiation caused the most significant changes in surface temperature.

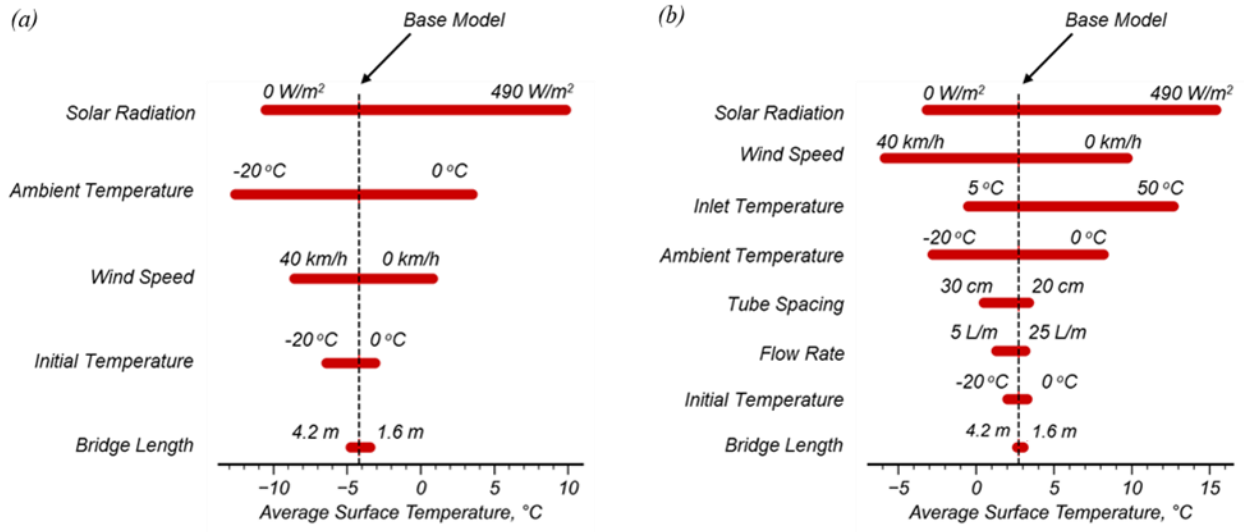


Figure 21: Effect of various parameters on bridge deck average surface temperature: (a) without tubing, and (b) with tubing

Step 2: Data Generation

The second step involved generating a comprehensive dataset through numerical simulation. The validated COMSOL model was used in conjunction with LiveLink for MATLAB to automate simulations across a wide range of input combinations. To capture realistic boundary conditions, environmental data were obtained from MDT's RWIS stations and analyzed statistically. Figure 22 presents histograms of key variables—ambient temperature, wind speed, solar radiation, and inlet fluid temperature—used to inform simulation inputs. For each variable, appropriate probability distributions were fitted, and the 1st, 5th, 95th, and 99th percentiles were extracted from both empirical and fitted distributions to define representative input ranges (see Table 4).

Ambient temperatures during winter months range from –35 °C to 0 °C, with a strong skew toward higher values. Approximately 95% of observed values fall above –25 °C, and 50% exceed

–10 °C. Wind speeds are mostly below 20 km/h, with over 90% of observations under this threshold, indicating moderate convective heat loss is typical. Solar radiation varies widely between 0 and 350 W/m², with a mode near 60 W/m², reflecting frequent overcast conditions during winter.

Inlet fluid temperatures show a clear bimodal distribution, reflecting geothermal heterogeneity across the state. One peak centers near 10 °C, consistent with shallow ground heat, while a second peak around 50 °C represents geothermal hot spring sources. Each mode was fit using separate normal distributions, and the corresponding mean and standard deviation values are listed in Table 5.

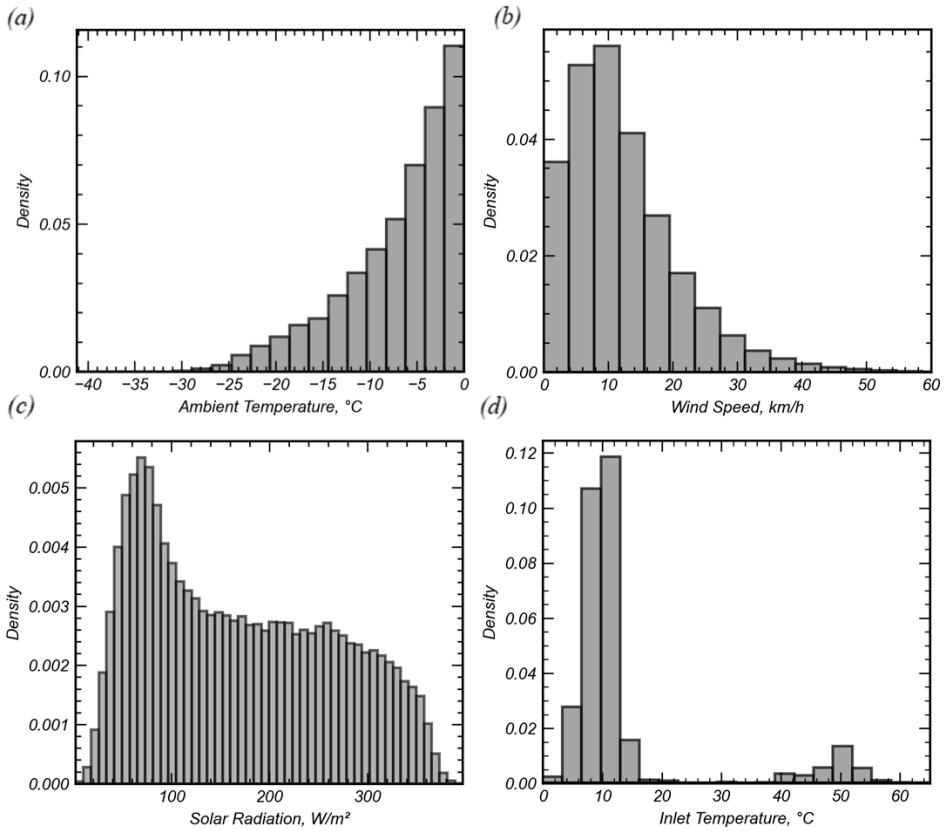


Figure 22: Distribution histograms of important features, a) Ambient temperature, b) Wind speed, c) Solar radiation, and d) Inlet temperature

Table 4: Different levels of percentiles for empirical values and fitted distributions for ambient temperature, wind speed, and solar radiation

Parameter	***Value***			
Empirical Values	1st Percentile	5th Percentile	95th Percentile	99th Percentile
Ambient Temperature, °C	-24.31	-19.48	-0.44	-0.08
Wind Speed, km/h	0.36	1.56	28.86	40.91
Solar Radiation, W/m^2	25.84	42.09	335.03	361.28
Fitted Distribution				
Ambient Temperature, °C	-32.43	-21.10	-0.36	-0.07
Wind Speed, km/h	0.45	1.57	28.97	37.85
Solar Radiation, W/m^2	25.58	42.28	359.12	461.46

Table 5: Mean and standard deviation of fitted distributions for inlet temperature

Parameter	***Value***	
Inlet Temperature	1st Distribution	2nd Distribution
Means of Fitted Distributions, °C	9.26	48.57
Standard Deviations of Fitted Distributions, °C	2.61	5.11

For design-related variables such as bridge deck length, tube spacing, and fluid flow rate, the parameter bounds were selected based on the results of the parametric sensitivity analyses presented in Chapter 2. These ranges were chosen to capture realistic design scenarios while ensuring sufficient resolution across the design space. The finalized ranges were used to construct a comprehensive input matrix for numerical simulations. In total, 555 simulations were performed for the *without tubing* configuration, varying key environmental parameters including ambient temperature (0 to –20 °C), wind speed (0–40 km/h), solar radiation (0–490 W/m²), and initial surface temperature (±10 to 20 °C relative to ambient), as summarized in Table 6.

Table 6: Parameter ranges, combinations and total number of models for generating the dataset without tubing from the numerical model

Parameter	***Value***	
	Range	Values
Ambient Temperature, ^{o}C	0 to -20	0, -5, -10, -15, -20
Initial Temperature, ^{o}C	-10 to +20 of Ambient Temperature	-10, -5, 0, 5, 10, 20 of Ambient Temperature
Wind Speed, km/h	0 to 40	0, 5, 10, 20, 30, 40
Solar Radiation, W/m^2	0 to 490	0, 160, 260, 360, 490
Bridge Length, m	1.6 to 4.8	1.6, 3.2, 4.8
Total Number of Models	**555**	

For the *with tubing configuration*, 1,836 simulations were conducted, incorporating additional system parameters such as inlet fluid temperature (8–50 °C), flow rate (5–25 L/min), and tube spacing (20–30 cm), while keeping consistent ranges for environmental inputs. Table 7 details the full parameter set and discretized input values used in the simulations. These simulations form a rich dataset for evaluating system performance under diverse operating conditions, enabling robust evaluation of de-icing effectiveness and informing the development of predictive models and design optimization strategies

Table 7: Parameter ranges, combinations and total number of models for generating the dataset with tubing from the numerical model

Parameter	***Value***	
	Range	Values
Ambient Temperature, ^{o}C	0 to -20	0, -5, -10, -15, -20
Initial Temperature, ^{o}C	-10 to +20 of Ambient Temperature	-10, -5, 0, 5, 10, 20 of Ambient Temperature
Wind Speed, km/h	0 to 40	0, 5, 10, 20, 30, 40
Solar Radiation, W/m^2	0 to 490	0, 160, 260, 360, 490
Inlet Temperature, ^{o}C	8 to 50	8, 10, 50
Fluid Flowrate, L/min	5 to 25	5, 10, 25
Tube Spacing, cm	20 to 30	20, 30
Bridge Length, m	1.6 to 4.8	1.6, 3.2, 4.8
Total Number of Models	**1836**	

Step 3: Data Splitting and Experimental Design

The generated dataset was divided into a training set (80%) and a testing set (20%) to ensure unbiased model evaluation. To improve generalizability and prevent overfitting, a 5-fold cross-validation scheme was implemented, where the training data were further divided into five subsets. Each model was trained on four folds and validated on the fifth, rotating through all folds. This approach ensured robust estimation of performance metrics across unseen data.

Step 4: Model Selection and Training

Two types of machine learning models were developed to meet different prediction objectives. The selected input features and target variables are shown in Table 8.

Table 8: Input features and target variables for machine learning model 1 and model 2

Features	***Targets***	
	Model 1	Model 2
Ambient Temperature, ^{o}C	- Stabilized Temperature - Time to Reach Above 0^{o}C - Time to Reach Stabilized Temperature	- Average Surface Temperature (every 0.1 hours interval)
Initial Temperature, ^{o}C		
Wind Speed, km/h		
Solar Radiation, W/m^{2}		
Inlet Temperature, ^{o}C		
Fluid Flowrate, L/min		
Tube Spacing, cm		
Bridge Length, m		

Figure 23 presents a schematic definition of three key system performance indicators used in Model 1: stabilized surface temperature (T_f), time to reach stabilized temperature (t_s), and time to reach above 0 °C (t_o). T_f is defined as the surface temperature at the point where its rate of change remains below 0.5% over three consecutive hours, indicating thermal equilibrium, while t_s is the duration required for the system to reach this steady-state condition. t_o quantifies how quickly the surface reaches the threshold required for ice melting.

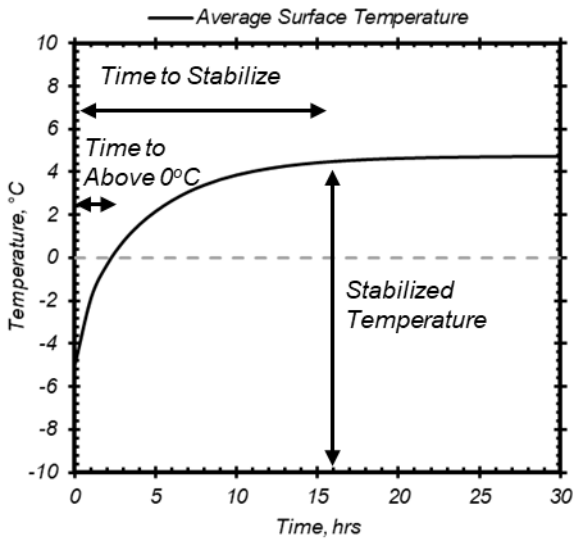


Figure 23: Schematic for stabilized temperature, time to reach stabilized temperature, and time to reach above 0°C

Model 2 was constructed to provide granular predictions of surface temperature at every 0.1-hour interval throughout the simulation period. This model used the same input features but replaced high-level targets with full temperature time series as the prediction output (Figure 24). Model 2 enables dynamic thermal profile monitoring and is particularly useful for forecasting thermal behavior under changing conditions.

Model 1 Output

- Stabilized Temperature = 4.5°C
- Time to Reach Stabilized Temperature = 16.8 hrs
- Time to Reach Above 0°C = 4.6 hrs

Model 2 Output

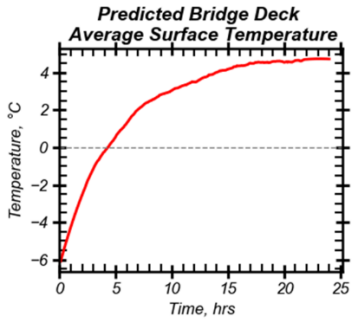


Figure 24: Outputs from Model 1 and Model 2

A key innovation in Model 2 was its adaptive time-stepping mechanism. When environmental or operational conditions changed, the model treated the last predicted surface temperature as the new initial condition and reset the simulation clock to zero. This allowed the model to capture the rapid response typically observed after condition changes, before the system reaches thermal equilibrium.

Step 5: Model Evaluation

The predictive performance of both Model 1 and Model 2 was evaluated using the following metrics:

Mean Absolute Error (MAE): is a widely used regression metric that quantifies the average magnitude of prediction errors, regardless of direction. It is defined as:

$$\text{MAE} = \frac{1}{n} \Sigma \, |y_i - \hat{y}_i| \tag{7}$$

where, y_i is the actual (true) value, $\hat{y}_i$ represents the predicted value from the machine learning model, and n is the total number of data points. MAE measures the mean absolute difference between predicted and actual values, offering an intuitive indication of model accuracy. Because it treats all errors equally, without squaring them, MAE is less sensitive to outliers compared to metrics like RMSE. This property makes it particularly suitable for evaluating models where consistent predictive performance is desired across a broad range of scenarios.

Root Mean Squared Error (RMSE): is a standard metric used to evaluate the predictive accuracy of regression models by measuring the square root of the average squared differences between predicted and actual values. It is defined as:

$$\text{RMSE} = \sqrt{\frac{1}{n}\,\Sigma\,(y_i - \hat{y}_i)^2} \tag{8}$$

where, y_i is the actual (true) value, $\hat{y}_i$ represents the predicted value from the machine learning model, and n is the total number of data points. Unlike MAE, RMSE penalizes larger errors more heavily due to the squaring operation, making it particularly sensitive to outliers and useful for identifying models that fail under extreme conditions. Additionally, RMSE is differentiable, which makes it well-suited as a loss function during model training. Since its units match those of the target variable, RMSE provides an interpretable measure of model performance in real-world physical systems.

Coefficient of Determination (R^2): measures the proportion of variance in the observed data that is captured by the model's predictions. It is defined as

$$R^2 = 1 - \frac{\Sigma\,(y_i - \hat{y}_i)^2}{\Sigma\,(y_i - \bar{y})^2} \tag{9}$$

where, y_i is the actual (true) value, $\hat{y}_i$ represents the predicted value from the machine learning model, and $\bar{y}$ is the mean of the actual values. R^2 ranges from 0 to 1, with higher values indicating better model performance. An R^2 value near 1 implies that the model accounts for most of the variability in the target data, while a value near 0 suggests poor predictive alignment. As a relative metric, R^2 is particularly useful for comparing the explanatory power of different models or configurations under the same dataset.

Model 1

a) Without Tubing: Figure 25 and Table 9 summarize the performance of various machine learning models—Linear Regression (LR), Polynomial Regression (PR), Decision Tree (DT), Random Forest (RF), XGBoost (XGB), and Fully Connected Neural Network (FCNN)—in

predicting three key performance indicators: stabilized surface temperature, time to reach above 0 °C, and time to reach thermal stabilization. The metrics reported include MAE, RMSE, and R^2.

In terms of MAE, XGBoost model demonstrates low average prediction errors across all three targets. For stabilized temperature, XGBoost reports the lowest MAE at 0.54, followed closely by FCNN at 0.56. For time to >0°C, where XGBoost again has the lowest MAE of 0.24, while decision tree yields a slightly higher value of 0.35. For time to stabilize, both XGBoost and decision tree record an MAE of 1.13 indicating their relative reliability in minimizing average prediction error.

With regard to RMSE, which emphasizes larger deviations and provides a more sensitive measure of prediction robustness, FCNN achieves the lowest RMSE for stabilized temperature at 0.78, suggesting stable and accurate prediction with minimal large errors. Meanwhile, XGBoost produces the lowest RMSE for time to >0°C and time to stabilize, at 0.86 and 2.74 respectively. These results imply that XGBoost may offer more consistent performance when predicting temperature transitions over time, particularly in contexts where larger errors are more consequential.

Looking at the coefficient of determination (R^2), FCNN achieves the highest values for stabilized temperature with an R^2 of 98.59%. While XGBoost has the highest values for two other target variables. It attains R^2 of 95.85% for time to >0°C, and an R^2 of 87.91% for time to stabilize indicating strong explanatory power and an ability to capture most of the variance in the data. Overall, both models, FCNN and XGBoost exhibit strong predictive capabilities, with FCNN performing well on steady-state temperature predictions, while XGBoost shows strength in capturing temporal stabilization trends.

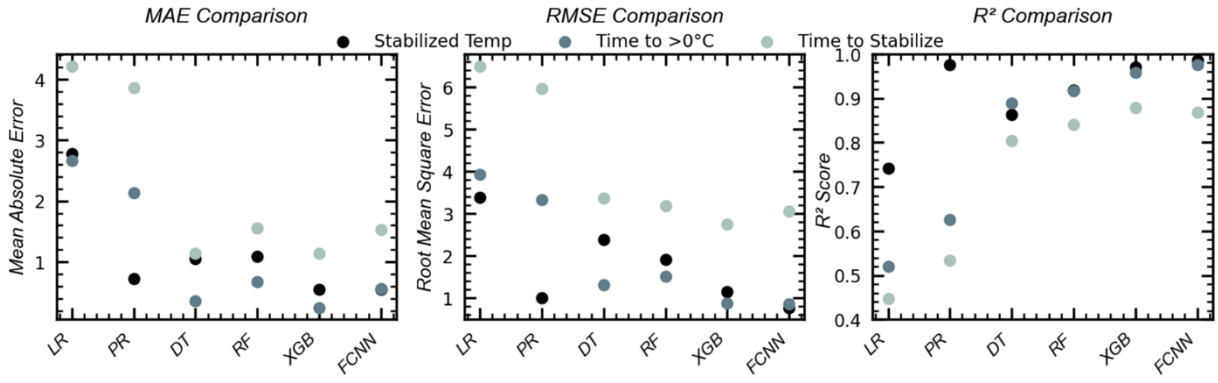


Figure 25: MAE, RMSE, and R^2 score comparison for Model 1 without tubing for Stabilized temperature, time to reach stabilized temperature, and time to reach above 0°C

Table 9: MAE, RMSE, and R^2 score values for Model 1 without tubing for Stabilized temperature, time to reach stabilized temperature, and time to reach above 0°C

Parameter	***Value***		
Mean Absolute Error	Stabilized Temp.	Time to > 0°C	Time to Stabilize
Linear Regression	2.77	2.66	4.21
Polynomial Regression	0.72	2.13	3.85
Decision Tree	1.05	0.35	1.13
Random Forest	1.09	0.67	1.55
XGBoost	0.54	0.24	1.13
Fully Connected Neural Network	0.56	0.60	1.70
Root Mean Squared Error			
Linear Regression	3.38	3.92	6.49
Polynomial Regression	0.99	3.33	5.95
Decision Tree	2.38	1.30	3.35
Random Forest	1.91	1.50	3.17
XGBoost	1.14	0.86	2.74
Fully Connected Neural Network	0.78	1.10	3.30
R^2 Score (%)			
Linear Regression	74.25	51.98	44.66
Polynomial Regression	97.63	62.62	53.38
Decision Tree	86.34	88.96	80.43
Random Forest	91.76	91.64	84.10
XGBoost	96.97	95.85	87.91
Fully Connected Neural Network	98.59	95.60	83.54

b) With Tubing: Figure 26 and Table 10 present the comparative performance of machine learning models for predicting stabilized surface temperature, time to reach above 0 °C, and time

to reach stabilization, under configurations where tubing is included in the system. The metrics reported include MAE, RMSE, and R^2.

In terms of MAE, XGBoost demonstrates the lowest average errors across multiple targets. It records an MAE of 0.22 for stabilized temperature and 0.73 for time to >0°C, indicating minimal average deviation from actual values in both early and steady-state phases. For time to stabilize, random forest achieves the lowest MAE of 1.14, closely followed by XGBoost at 1.17, suggesting that both models provide comparable accuracy in predicting the longer stabilization period.

For RMSE, XGBoost yields the lowest values for all three target variables. It reports an RMSE of 0.46 for stabilized temperature, 1.75 for time to >0°C, and 2.39 for time to stabilize. These lower RMSE values indicate that XGBoost predictions are not only accurate on average but also less affected by large individual errors, making the model more robust in scenarios where minimizing significant deviations is critical.

With respect to the coefficient of determination (R^2), XGBoost achieves the highest value for time to >0°C at 83.52%, suggesting it captures a substantial portion of the variance in this early-phase response. For time to stabilize, random forest shows the highest R^2 at 79.84%, though XGBoost follows closely at 79.61%, indicating similar explanatory power. For stabilized temperature, XGBoost attains an R^2 of 99.66%, reflecting its effectiveness in modeling the final steady-state condition of the system.

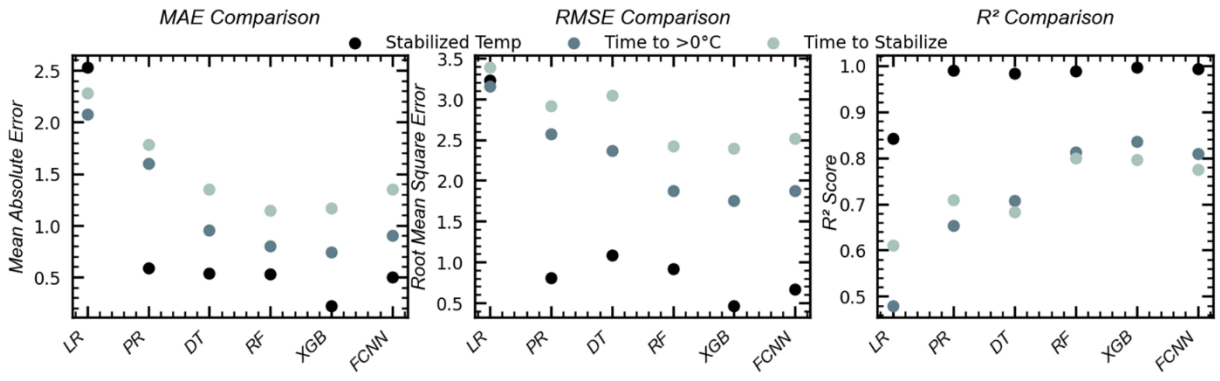


Figure 26: MAE, RMSE, and R^2 score comparison for Model 1 with tubing for Stabilized temperature, time to reach stabilized temperature, and time to reach above 0ºC

Table 10: MAE, RMSE, and R^2 score values for Model 1 with tubing for Stabilized temperature, time to reach stabilized temperature, and time to reach above 0ºC

Parameter	***Value***		
Mean Absolute Error	Stabilized Temp.	Time to > 0°C	Time to Stabilize
Linear Regression	2.53	2.07	2.28
Polynomial Regression	0.58	1.59	1.78
Decision Tree	0.53	0.95	1.35
Random Forest	0.52	0.80	1.14
XGBoost	0.22	0.73	1.17
Fully Connected Neural Network	0.44	0.91	1.30
Root Mean Squared Error			
Linear Regression	3.22	3.15	3.39
Polynomial Regression	0.80	2.56	2.91
Decision Tree	1.08	2.36	3.04
Random Forest	0.91	1.87	2.41
XGBoost	0.46	1.75	2.39
Fully Connected Neural Network	0.59	1.89	2.41
R^2 Score (%)			
Linear Regression	84.19	48.00	61.08
Polynomial Regression	99.02	65.28	70.92
Decision Tree	98.21	70.71	68.33
Random Forest	98.71	81.31	79.84
XGBoost	99.66	83.52	79.61
Fully Connected Neural Network	99.45	79.66	78.53

Due to the relatively simple nature of the target variables in Model 1, particularly the stabilized surface temperature, which is a single-value summary of the full thermal response, most machine learning models were able to achieve higher R^2 scores when predicting this metric.

Model 2

a) Without Tubing: Figure 27 and Table 11 present a performance comparison of various machine learning models for Model 2 output without tubing, evaluated using MAE, RMSE, and R^2.

In terms of MAE, the fully connected neural network (FCNN) reports the lowest value at 0.29, followed by XGBoost at 0.37. These low MAE values indicate that both models consistently produce predictions with small average deviations from the actual values. Other models, including polynomial regression (0.89), decision tree (0.51), and random forest (0.61), also perform reasonably well, while linear regression shows a substantially higher MAE of 2.93, indicating the non-linearity relationships that were not captured by the linear model.

RMSE values further highlight the performance differences across models, especially with respect to the penalization of larger errors. The FCNN achieves the lowest RMSE at 0.41, suggesting strong robustness against extreme deviations. XGBoost follows with an RMSE of 0.90, also reflecting consistent performance. Polynomial regression and random forest share an RMSE of 1.22, while decision tree and linear regression show higher values at 1.50 and 3.93, respectively.

Regarding the coefficient of determination (R^2), FCNN attains the highest value at 99.79%, indicating that it explains nearly all of the variance in the observed data. XGBoost also achieves a high R^2 score of 99.17%, showing its strong predictive capability. Polynomial regression (98.69%), random forest (98.46%), and decision tree (97.56%) all demonstrate good explanatory power,

while linear regression lags behind with an R^2 of 86.31%. These results show that both FCNN and XGBoost offer accurate and consistent predictions, making them more suitable for modeling system behavior in the absence of tubing.

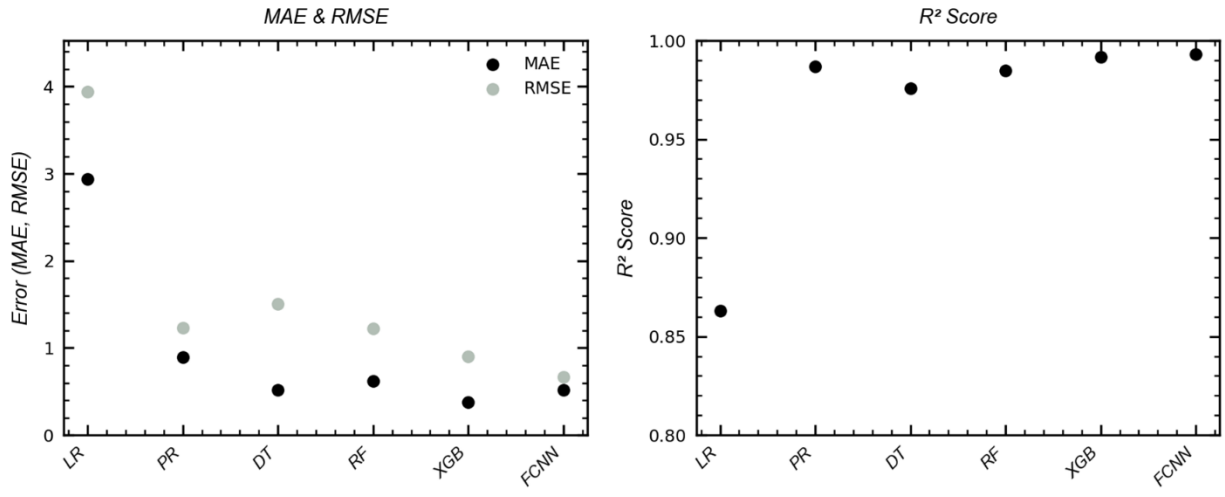


Figure 27: MAE, RMSE, and R^2 score comparison for Model 2 output without tubing

Table 11: MAE, RMSE, and R^2 score values for Model 2 output without tubing

Parameter	***Value***		
	MAE	RMSE	R^2 Score (%)
Linear Regression	2.93	3.93	86.31
Polynomial Regression	0.89	1.22	98.69
Decision Tree	0.51	1.50	97.56
Random Forest	0.61	1.22	98.46
XGBoost	0.37	0.90	99.17
Fully Connected Neural Network	0.29	0.41	99.79

In the case of Model 2 without tubing, the surface temperature profiles were comparatively simpler to predict due to the reduced number of influencing parameters and the absence of active heating effects. As a result, the temperature trends exhibited smoother and more predictable behavior over time. This simplicity allowed most machine learning models to perform well, achieving relatively high predictive accuracy even with less complexity.

b) With Tubing: Figure 28 and Table 12 present the model performance comparison for Model 2 output with tubing, evaluated using MAE, RMSE, and R^2 score.

In terms of MAE, the fully connected neural network (FCNN) demonstrates the lowest error at 0.64, indicating minimal average deviation between predicted and actual values. XGBoost follows closely with an MAE of 0.68, also reflecting high predictive accuracy. Random forest (0.91), polynomial regression (1.06), and decision tree (1.09) show moderate average errors, while linear regression reports the highest MAE of 3.23, suggesting weaker performance in modeling the system with tubing.

RMSE values further differentiate the models based on their sensitivity to larger errors. FCNN records the lowest RMSE at 2.26, suggesting strong robustness and reduced influence from outliers or large deviations. XGBoost again performs well with an RMSE of 2.57, followed by polynomial regression at 2.74. In contrast, random forest (3.28), decision tree (4.45), and linear regression (4.77) show higher RMSE values, indicating more pronounced larger prediction errors.

For the coefficient of determination (R^2), FCNN achieves the highest score at 95.79%, reflecting its strong ability to explain the variance in the data. XGBoost also shows a high R^2 value of 94.29%, while polynomial regression (93.52%) and random forest (90.83%) perform slightly lower. Decision tree and linear regression record R^2 scores of 83.05% and 84.11%, respectively. These results indicate that both FCNN and XGBoost offer consistent and accurate predictions for system behavior with tubing, supported by high variance explanation and low error metrics.

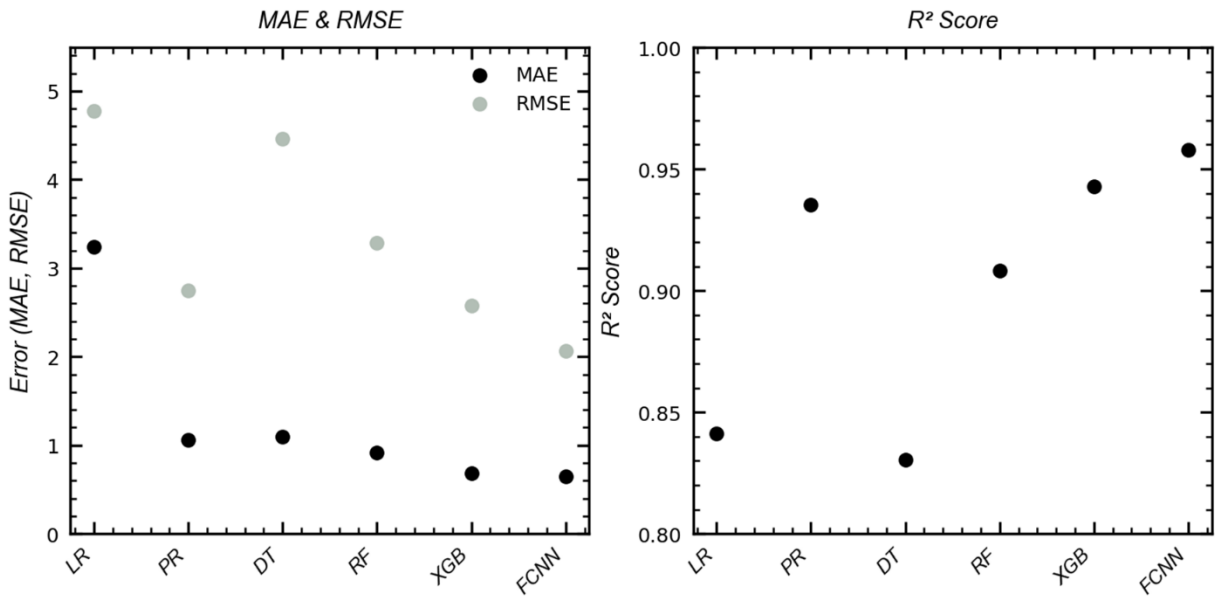


Figure 28: MAE, RMSE, and R^2 score comparison for Model 2 output with tubing

Table 12: MAE, RMSE, and R^2 score values for Model 2 output with tubing

Parameter	***Value***		
	MAE	RMSE	R^2 Score (%)
Linear Regression	3.23	4.77	84.11
Polynomial Regression	1.06	2.74	93.52
Decision Tree	1.09	4.45	83.05
Random Forest	0.91	3.28	90.83
XGBoost	0.68	2.57	94.29
Fully Connected Neural Network	0.64	2.26	95.79

Given its detailed and dynamic predictions, Model 2 using the FCNN architecture was selected as the preferred model for subsequent analysis and application.

Step 6: Feature Importance Analysis

To evaluate the relative importance of each input feature on the model's predictive performance, permutation feature importance was applied to the fully connected neural network (FCNN). In this method, the trained FCNN model was kept fixed, and the input validation dataset

was systematically perturbed. For each feature, its values were randomly shuffled across all samples, effectively disrupting the original relationship between that feature and the target variable, while leaving all other features unchanged. The perturbed input dataset was then fed through the FCNN to generate new predictions. The mean absolute error (MAE) was computed for each perturbed case and compared to the baseline MAE obtained using the unaltered dataset. The increase in MAE after permuting a given feature quantifies the loss of predictive accuracy caused by breaking the feature-target relationship, and thus serves as a direct measure of that feature's importance. Features causing greater degradation in model performance were considered more influential. Finally, the importance scores were normalized to enable comparison across features and visualized using a radar plot.

The results, shown in Figure 29, highlight that Inlet Temperature, Ambient Temperature, Wind Speed, and Solar Radiation are the most critical features affecting surface temperature predictions. Initial Temperature showed moderate importance, while Bridge Length, Tube Spacing, and Flowrate had the least influence on model predictions. This aligns with prior sensitivity findings and underscores the physical relevance of the selected inputs.

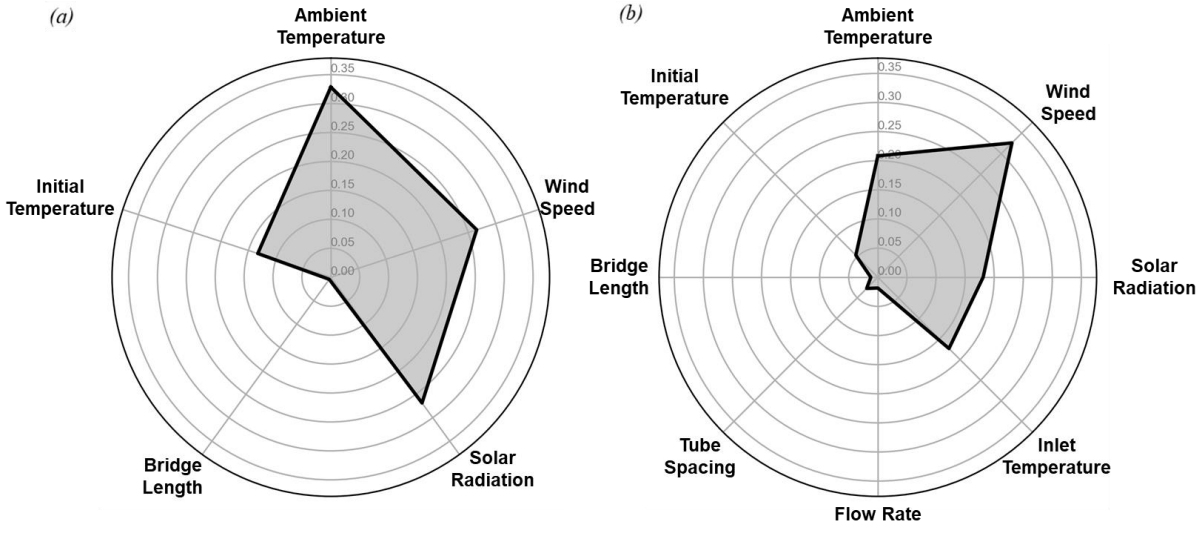


Figure 29: Permutation-based feature importance for FCNN model predictions visualized as radar plot: a) without tubing, and b) with tubing

Temperature Prediction Interactive Tool

To support practical deployment and real-time decision-making, an interactive tool was developed that integrates a trained fully connected neural network (FCNN) with a web-based interface. The tool features an embedded interactive map of Montana that displays the geographic locations of all bridge decks analyzed in this study. When a user selects a specific bridge location on the map, the tool retrieves and displays the live ambient temperature (°C), wind speed (km/h), and solar radiation (W/m²) for that site, using real-time weather data sources. Figure 30 shows the interactive map interface with bridge locations across Montana.

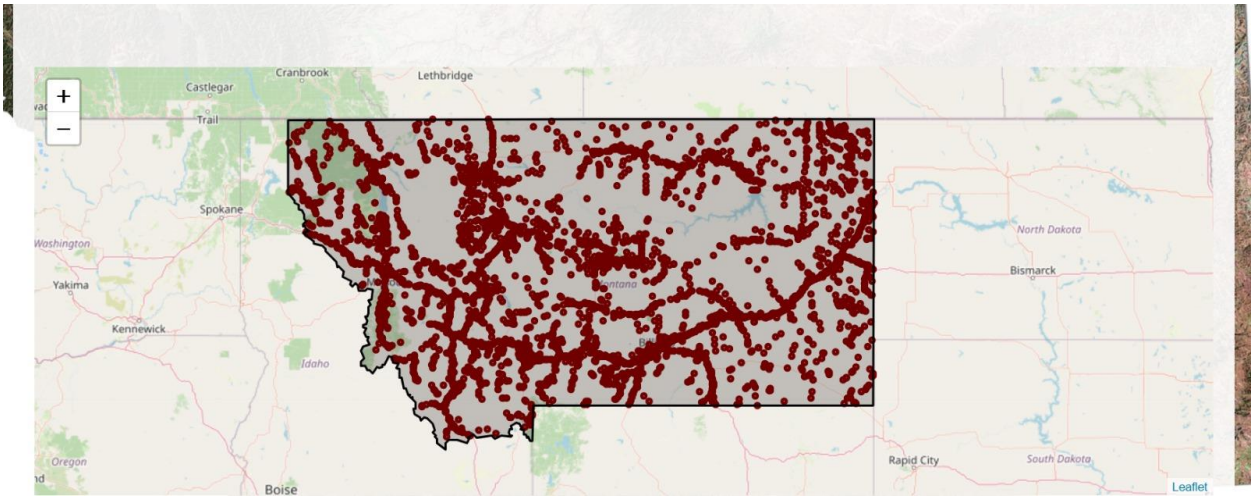


Figure 30: Interactive map of Montana showing bridge deck locations

The core of the tool is the embedded FCNN model, which predicts bridge deck surface temperature under various design and environmental conditions. Users are prompted to specify two types of input parameters: (1) fixed values that remain constant throughout the simulation and (2) time-varying values that may change during the prediction window. The fixed parameters

include bridge length (m), initial surface temperature (°C), inlet fluid temperature (°C), flow rate (L/min), and tube spacing (cm). The tool also allows users to choose between the "with tubing" or "without tubing" configurations to reflect different design scenarios. Figures 31(a) and 31(b) display the fixed and variable input sections of the tool interface, respectively.

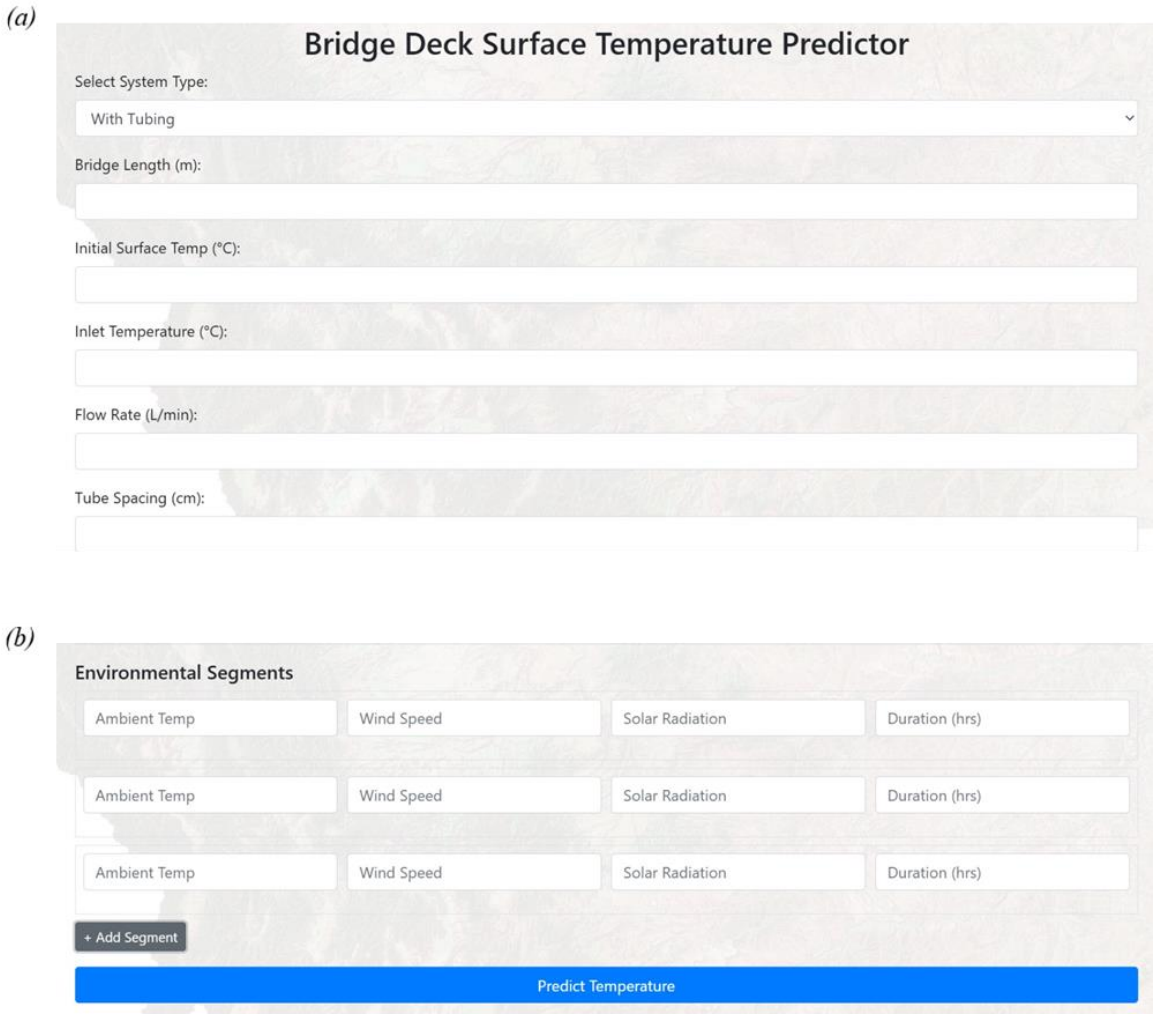


Figure 31: Input parameters interface for: (a) fixed parameters, and (b) variable parameters

For the time-varying parameters, the user provides a sequence of ambient temperature (°C), wind speed (km/h), and solar radiation (W/m²) values, along with the duration (hours) for which each set of conditions remains constant. The tool supports the addition of an unlimited number of

segments, allowing users to simulate realistic environmental transitions over time. For each segment, the model uses the ending surface temperature of the previous segment as the initial condition for the next. This sequential logic ensures that transient effects and thermal lag are appropriately captured. Once the input is defined, the tool predicts and plots the surface temperature versus time, enabling dynamic evaluation of system behavior.

Figure 32 presents the prediction output for a two-segment scenario under the "with tubing" condition, with a bridge length of 1.5 m, initial surface temperature of −10°C, inlet temperature of 10°C, flow rate of 25 L/min, and tube spacing of 20 cm. The first segment simulates 12 hours of conditions with ambient temperature of −10°C, wind speed of 10 km/h, and solar radiation of 0 W/m². The second segment maintains the same ambient temperature and wind speed but increases the solar radiation to 490 W/m², sustained for an additional 12 hours. The output plot visualizes how the surface temperature evolves in response to these environmental changes.

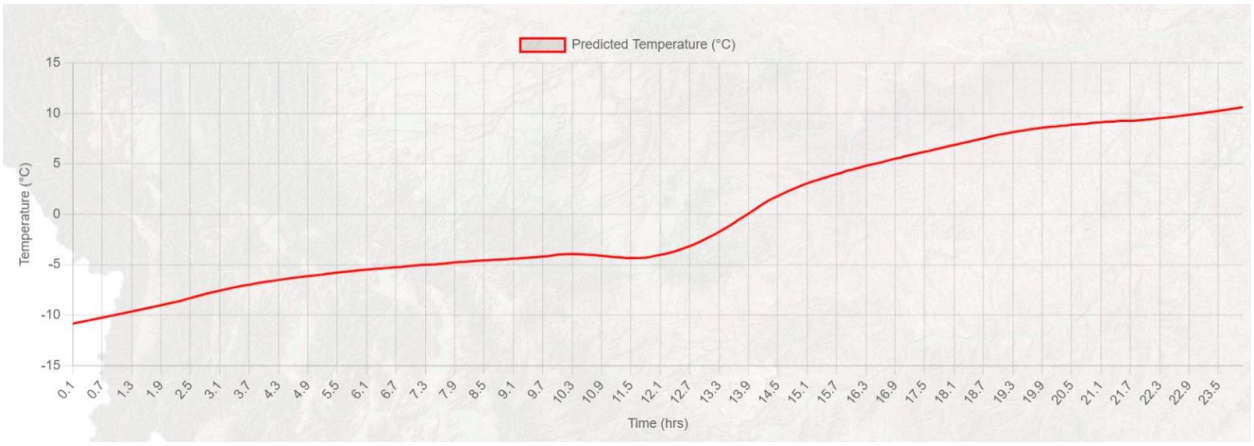


Figure 32: Predicted surface temperature over time for a two-segment “with tubing” scenario

Summary

This chapter presented the development of a machine learning (ML)-based predictive framework to simulate the thermal behavior of geothermal bridge deck systems, building upon the validated numerical model from Chapter 2. The primary motivation for this work was to create a tool capable of rapidly predicting bridge deck surface temperatures for a wide range of environmental and design conditions, with the ultimate goal of improving roadway safety during winter months. By enabling precise evaluation of surface conditions, the framework aims to support proactive deicing strategies and help maintain safer transportation infrastructure during cold weather events. The model development process followed a structured six-step approach: (1) feature selection, (2) data generation, (3) data splitting and experimental design, (4) model selection and training, (5) model evaluation, and (6) sensitivity analysis. Parametric studies informed the selection of key input features, and over 2,000 numerical simulations were conducted to generate the training dataset. Two models were developed: Model 1 predicted system responses (stabilized temperature, time to >0°C, time to stabilization), while Model 2 provided continuous surface temperature predictions at 0.1-hour intervals. A range of supervised learning algorithms, including linear models, decision trees, ensemble methods, and fully connected neural networks (FCNN), were implemented and evaluated using standard metrics (MAE, RMSE, and R^2). Model performance varied across tasks and configurations. For Model 1, XGBoost demonstrated strong performance for predicting time-dependent outputs, while FCNN performed well for stabilized temperature predictions. For Model 2, FCNN better compared to other models in terms of accuracy and variance explanation, especially under more complex “with tubing” scenarios. Feature importance analysis using a permutation-based method identified inlet temperature, ambient temperature, wind speed, and solar radiation as the most influential parameters, consistent with

earlier parametric analyses. The results demonstrate that the developed ML framework offers a reliable, interpretable, and efficient alternative to conventional simulation-based evaluations for geothermal bridge deck systems.

Future Work

Several promising directions can be pursued to enhance the machine learning framework developed in this chapter. One important area involves incorporating additional environmental and site-specific factors that influence the thermal behavior of bridge decks. Variables such as precipitation and snow accumulation could further refine the prediction of surface temperatures under real-world conditions. Integrating these parameters would not only improve model precision but also support more comprehensive winter maintenance strategies by accounting for moisture-related heat exchange and insulation effects. Additionally, future work may explore the influence of surrounding topography, shading effects, or traffic-induced convective heat transfer, which are often overlooked in traditional models but may influence microclimate and heat retention around bridge structures. Another valuable extension involves integrating probabilistic modeling techniques and uncertainty quantification into the current framework. While the existing models provide deterministic predictions, they do not account for variability in input conditions, data uncertainty, or model limitations. Developing a probabilistic prediction framework would enable stakeholders to evaluate the confidence level associated with each forecast and perform risk-informed decision-making. This would be especially useful in scenarios where safety margins are critical or environmental inputs are uncertain. Monte Carlo simulations, Bayesian methods, or ensemble modeling approaches could be employed to assess the range and likelihood of possible outcomes under varying input scenarios. Building on these advancements, a major future direction

is the development of an interactive, real-time feasibility mapping system. By leveraging live weather data from RWIS stations, satellite observations, and embedded sensor networks, surface temperature predictions could be dynamically updated across the state. When combined with geospatial data on ground thermal properties, bridge geometry, and traffic demand, the ML models could drive a GIS-based platform that visualizes deicing feasibility in real time. Such a tool would provide transportation agencies with actionable insights for prioritizing bridge retrofits, allocating heating resources, and mitigating hazardous conditions during winter months. This approach would support data-driven infrastructure planning and help extend the ML framework into practical, operational contexts.

REFERENCES CITED

Baboian, R. (1992). Synergistic effects of acid deposition and road salts on corrosion. In *Corrosion forms and control for infrastructure* (pp. 17-29). ASTM International.

Bowers, G. (2016). Ground-source bridge deck deicing and integrated shallow geothermal energy harvesting systems [*Doctoral dissertation, Virginia Tech*].

Casasso, Alessandro, and Rejandrea Sethi. 2016 “G.POT: A Quantitative Method for the Assessment and Mapping of the Shallow Geothermal Potential.” Science Direct.

COMSOL. (2017). “COMSOL MultiphysicsTM Version 5.3: Pipe Flow Module User’s Guide.” COMSOL Inc., Burlington, MA.

COMSOL. (2018a). “COMSOL MultiphysicsTM Version 5.4: Heat Transfer Module User’s Guide.” COMSOL Inc., Burlington, MA.

COMSOL. (2018b). “COMSOL MultiphysicsTM Version 5.4: Structural Mechanics Module User’s Guide.” COMSOL Inc., Burlington, MA.

EPA. 2018 “Greenhouse Gas Emissions from a Typical Passenger Vehicle.” Environmental Protection Agency, Office of Transportation and Air Quality.

Erickson, Kay. 2018 “State Plows through Budget to Maintain Montana Roads This Winter.” YPR, KEMC.

Fay, Laura, et al. 2015 “Benefit-Cost of Various Winter Maintenance Strategies - Clear Roads.” Clear Roads, Western Transport Institute.

Feng, J., & Yin, G. (2019). Thermal Analyses and Responses of Bridge Deck Hydronic Snow Melting System. *Advances in Civil Engineering, 2019*.

Fischel, M. (2001). Evaluation of selected deicers based on a review of the literature. *CDOT-DTD-R-2001-15*, 160. (*Colorado Department of Transportation*).

Fliegel, J., Flyer, J., Katz, M., Le, A., Ngo, T., Roberts, K., Santoro, A., Sun, C., & Weyforth, T. (2010). Design and evaluation of a retrofittable electric snow melting system for pavements (*Doctoral dissertation, University of Maryland*)

Ghasemi-Fare, O., Bowers, G. A., Kramer, C. A., Ozudogru, T. Y., Basu, P., Olgun, C. G., Bulbul, T., & Sutman, M. (2015). *A feasibility study of bridge deck deicing using geothermal energy*.

GWIC. (2022). Ground Water Wells. Montana Bureau of Mines and Geology

HIFLD. (2022). Electric Transmission Lines. Homeland Infrastructure Foundation-Level Data

Homeguide. 2022 “2022 Well Drilling Costs: Average Water Well Installation Cost.” HomeGuide.

Kusuda, T., & Achenbach, P. R. (1965). Earth temperature and thermal diffusivity at selected stations in the United States, National Bureau of Standards Gaithersburg MD (No. NBS-8972).

Liu, Hongwei, et al. 2018 “Feasibility Study of Snow Melting System for Bridge Decks Using Geothermal Energy Piles Integrated with Heat Pump in Canada.” Science Direct, Renewable Energy.

Liu, X. (2005). Development and experimental validation of simulation of hydronic snow melting systems for bridges [*Doctoral dissertation, Oklahoma State University*].

Lund, J., & Boyd, T. (2016). Direct utilization of geothermal energy 2015 Worldwide review. Geothermics, 60, pp. 66-93.

Mohammadzadeh, A., Jazi, F., Ghasemi-Fare, O., & Sun, Z. (2023). Analyzing the feasibility of using shallow geothermal energy to prohibit pavement thermal cracking: field testing. Geo-Congress 2023: Soil Improvement, Geoenvironmental, and Sustainability. https://doi.org/10.1061/9780784484661.063

Mathers, Jason, et al. 2019 “The Green Freight Handbook a Practical Guide for Developing a Sustainable Freight Transportation Strategy for Business.” 1Library, Environmental Defense Fund.

MDT. (2022). Bridge Locations. Montana Department of Transportation

MDT. (2022). Melting Sands and Plowing Miles. Montana Department of Transportation

MDT RWIS. (2022). Surface Temperature. Road Weather Information’s Systems Montana Department of Transportation

MDT RWIS. (2022). Wind Conditions. Road Weather Information’s Systems Montana Department of Transportation

MDT Web Administrators, 2019. (n.d.). Montana Department of Transportation. Deicing, Plowing & Sanding.

Montana Department of Transportation (2002). Montana structures manual – Part II. Retrieved from https://www.mdt.mt.gov/publications/manuals.aspx

Menerga En. 2020 “What Is Shallow Geothermal Energy and Why Should You Use It?” Menerga En, Menerga En.

NOAA. (2022). U.S. Climate Normals. National Centers for Environmental Information

Powell, Olivia. 2022 “The Cost of Drilling a Water Well in Montana.” Groundwater Covernance.

Raines, Gary L, and Bruce Johnson. 1996 “Digital Representation of the Montana State Geologic Map: A Contribution to the Interior Columbia River Basin Ecosystem Management Project.” Digital Representation of the Montana State Geologic Map: A Contribution to

the Interior Columbia River Basin Ecosystem Management Project | U.S. Geological Survey.

Ramos-Escudero, Adela, et al. 2021 “Evaluation of the Shallow Geothermal Potential for Heating and Cooling and Its Integration in the Socioeconomic Environment: A Case Study in the Region of Murcia, Spain.” MDPI, Multidisciplinary Digital Publishing Institute.

Ritter, Michael E. 2012 “Energy Balance.” Energy Balance, The Physical Environment.

Robertson, Eugene. 1988 “Thermal Properties of Rocks.” United States Department of the Interior Geological Survey.

Robinson, D. 2021. Icy Road Accident Statistics. Icy Road Safety.com - Prepare for Weather's Most Underrated Hazard. (n.d.).

Turner, E., Khosravi, M., Matteson, K., Plymesser, K., Toomani, P., McKittrick, L., Jackson, J., (2024). Application of geothermal bridge deck deicing systems to mitigate concrete deterioration from temperature fluctuation: model scale experiments. *Journal of Bridge Engineering 29 (8), 04024053.* https://ascelibrary.org/doi/epdf/10.1061/JBENF2.BEENG-6795

Turner, E., Khosravi, M., Toomani, P., Matteson, K., Plymesser, K., McKittrick, L., Jackson, J., (2024). Numerical evaluation of applying geothermal bridge deck deicing systems to mitigate concrete deterioration from temperature fluctuations. *Journal of Bridge Engineering 29 (10), 04024075.* https://ascelibrary.org/doi/epdf/10.1061/JBENF2.BEENG-6849

Shi, X., Du, S., & Fay, L. (2018). Environmental Risks of Snow and Ice Control Materials. *Sustainable Winter Road Operations,* 180-210.

USGS. (2022). Montana Hot Springs Locations. NOAA National Geophysical Data Center.

Williams, Dam. 2003 “PAST AND CURRENT PRACTICES OF WINTER MAINTENANCE AT THE MONTANA DEPARTMENT OF TRANSPORTATION (MDT).” Montana Department of Transportation, Mdt.

Yu, X., Puppala, A. J., & Zhang, N. (2017). Use of geothermal energy for deicing approach pavement slabs and bridge decks, phase 1. *Texas. Dept. of Transportation. Research and Technology Implementation Office,* No. FHWA/TX-18/0-6872-1.

APPENDICES

APPENDIX A

EXPERIMENTAL BRIDGE DECK SCHEMATIC

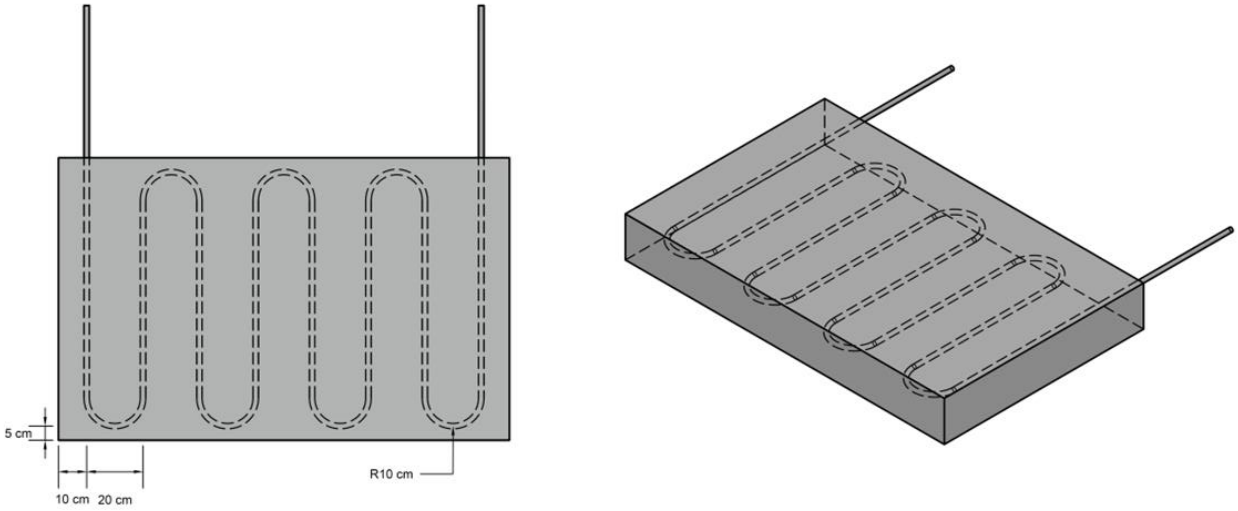


Figure A1: Tubing configuration in bridge deck a) top view, and b) 3D view

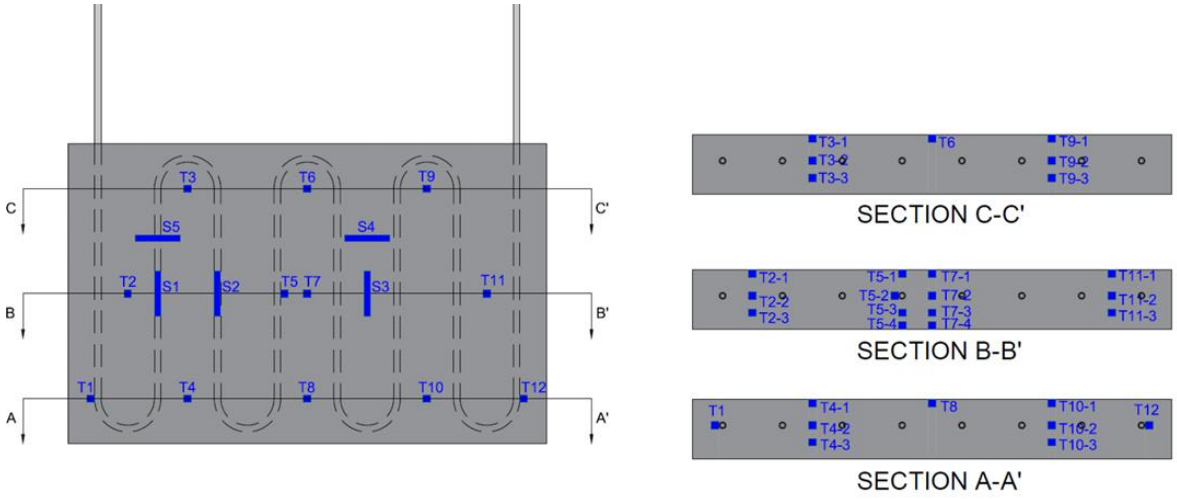


Figure A2: Sensor configuration in bridge deck a) top view, and b) cross section view

APPENDIX B

DETERMINISTIC ANALYSIS

Table B1: QBHE Variables

Parameter	***Values***	***Units***
T_{lim} *Cooling*	*-2*	*°C*
T_{lim} *Heating*	*20*	*°C*
L	*100*	*M*
R_b	*6.74e-2*	*mK/W*
t_C *Cooling*	*153*	*d*
t_C *Heating*	*212*	*d*
t_Y	*1*	*y*
t_S	*50*	*y*
r_b	*0.075*	*m*

Table B2: System Installation Costs

Parameter	***GSHP Installation Cost ($)***
Total Cost	*21,658,152*
Average Cost	*81,005*
Maximum Bridge cost	*101,394*
Minimum Bridge Cost	*57,894*

Table B3: Environmental Analysis Results

Environmental Analysis Parameter	***Total Bridges***	***Average Bridge***	***Units***
Amount of Melting Chlorides Used	*206.73*	*0.08*	*Tons*
Reduction in Total melting Chlorides	*23765.97*	*23972.62*	*Tons*
Percent decrease in Melting Chlorides	*0.86%*	*0.0003%*	*%*
CO_2 *Emissions*	*28.9932467*	*0.010863041*	*Tons*
CO_2 *Emission Reduction*	*3333.052253*	*3362.034637*	*Tons*
CO_2 *Percent Reduction*	*0.86%*	*0.0003%*	*%*